

# The Birth of an Ultra-Luminous X-ray Source in M83<sup>1</sup>

Roberto Soria<sup>2</sup>, K. D. Kuntz<sup>3</sup>, P. Frank Winkler<sup>4,7</sup>,  
William P. Blair<sup>3,7</sup>, Knox S. Long<sup>5,7</sup>, Paul P. Plucinsky<sup>6</sup>, and Bradley C. Whitmore<sup>5</sup>

## ABSTRACT

A previously undetected ( $L_X < 10^{36}$  erg s<sup>-1</sup>) source in the strongly star-forming galaxy M83 entered an ultraluminous state between August 2009 and December 2010. It was first seen with *Chandra* on 23 December 2010 at  $L_X \approx 4 \times 10^{39}$  erg s<sup>-1</sup>, and has remained ultraluminous through our most recent observations in December 2011, with typical flux variation of a factor of two. The spectrum is well fitted by a combination of absorbed power-law and disk black-body models. While the relative contributions of the models varies with time, we have seen no evidence for a canonical state transition. The luminosity and spectral properties are consistent with accretion powered by a black hole with  $M_{BH} \approx 40\text{--}100M_\odot$ . In July 2011 we found a luminous, blue optical counterpart which had not been seen in deep *HST* observations obtained in August 2009. These optical observations suggest that the donor star is a low-mass star undergoing Roche-lobe overflow, and that the blue optical emission seen during the outburst is coming from an irradiated accretion disk. This source shows that ultraluminous X-ray sources (ULXs) with *low-mass* companions are an important component of the ULX population in star-forming galaxies, and provides further evidence that the blue optical counterparts of some ULXs need not indicate a young, high-mass companion, but rather that they may indicate X-ray reprocessing.

---

<sup>2</sup>Curtin Institute of Radio Astronomy, Curtin University, 1 Turner Avenue, Bentley WA6102, Australia; roberto.soria@icrar.org

<sup>3</sup>The Henry A. Rowland Department of Physics and Astronomy, Johns Hopkins University, 3400 N. Charles Street, Baltimore, MD, 21218; kuntz@pha.jhu.edu, wpb@pha.jhu.edu

<sup>4</sup>Department of Physics, Middlebury College, Middlebury, VT, 05753; winkler@middlebury.edu

<sup>5</sup>Space Telescope Science Institute, 3700 San Martin Drive, Baltimore, MD, 21218; whitmore@stsci.edu, long@stsci.edu

<sup>6</sup>Harvard-Smithsonian Center for Astrophysics, 60 Garden Street, Cambridge, MA 02138; plucinsky@cfa.harvard.edu

<sup>7</sup>Visiting Astronomer, Gemini Observatory, La Serena, Chile

*Subject headings:* galaxies: individual (M83) – X-rays: binaries – black hole physics – accretion disks

## 1. Introduction

Point-like X-ray sources with luminosities exceeding the Eddington limit of normal stellar-mass black holes ( $L_X \gtrsim 3 \times 10^{39}$  ergs s<sup>-1</sup>, assuming isotropic emission) are commonly known as Ultraluminous X-ray sources (ULXs). The most luminous class of non-nuclear sources in galaxies, they are widely believed to result from some extreme form of accreting X-ray binary containing a black hole. However, the nature of both the black holes that power the ULXs and the companion stars that fuel them remain enigmatic. Briefly, the principal competing models for the primaries are: (a) intermediate (between normal stars and AGN) mass black holes ( $10^2 M_\odot \lesssim M_{\text{BH}} \lesssim 10^4 M_\odot$ ) perhaps formed in the collapsed core of massive star clusters—many of which are present in M83 (Colbert & Mushotzky 1999); (b) “normal” stellar-mass black holes ( $M_{\text{BH}} \lesssim 20 M_\odot$ ) that are accreting well above their Eddington limit (Begelman 2002) and/or that have beamed emission (*e.g.*, King et al. 2001; Begelman et al. 2006); and (c) “heavy” stellar black holes ( $M_{\text{BH}} \approx 30\text{--}70 M_\odot$ )—perhaps formed from direct collapse of metal-poor, massive stars (Belczynski et al. 2010; Zampieri & Roberts 2009; Pakull & Mirioni 2002)—that are accreting near or just above their Eddington limit.

A number of lines of evidence suggest that most ULXs are associated with young, high-mass stellar populations—the extreme of the high-mass X-ray binary (HMXB) population. Statistically, ULXs are found mostly in star-forming spirals or irregular galaxies (Irwin et al. 2004; Swartz et al. 2004) and the number of ULXs per galaxy increases with the star-formation rate (Colbert et al. 2004; Liu et al. 2006). The cumulative luminosity function for ULXs in star-forming galaxies is consistent with the extrapolation of that for HMXBs (Walton et al. 2011; Swartz et al. 2011). Within individual galaxies,  $\sim 75\%$  of ULXs are found in thin spiral arms and dust lanes, and tend to have high absorbing column densi-

---

<sup>1</sup>Based on observations made with NASA’s Chandra X-ray Observatory, the NASA/ESA Hubble Space Telescope, *Swift*, the 6.5 meter Magellan Telescopes located at Las Campanas Observatory, and the Gemini Observatory. NASA’s Chandra Observatory is operated by Smithsonian Astrophysical Observatory under contract # NAS83060 and the data were obtained through program GO1-12115. The *HST* observations were obtained at the Space Telescope Science Institute, which is operated by the Association of Universities for Research in Astronomy, Inc. (AURA), under NASA contract NAS 5-26555. The new *HST* observations were obtained through programs # GO-12513 and GO-12683. Data in the *HST* archive from program GO-11360 was also used. The ground-based observations were obtained through NOAO which is operated by Association of Universities for Research in Astronomy, Inc. for the National Science Foundation.

ties (Liu et al. 2006). Theoretical considerations suggest that high-mass donors can maintain a ULX in a persistent high state for up to 10 Myr (Rappaport et al. 2005).

Yet there is mounting evidence for a second population of ULXs, a population that represents an extreme form of low-mass X-ray binaries (LMXBs). The cumulative luminosity function of ULXs in elliptical galaxies is consistent with the extrapolation of the luminosity function for LMXBs (Swartz et al. 2004; Walton et al. 2011), suggesting that those ULXs are extreme LMXBs. In spiral galaxies, the number of ULXs is not purely a function of the star formation rate, but is also a function of the total stellar mass, suggesting that 15% to 25% of the total number of ULXs are associated with the older stellar population (Colbert et al. 2004; Liu et al. 2006; Winter et al. 2006; Mushotzky 2006).

Point-like, blue optical counterparts have been identified for a number of ULXs (*e.g.*, Ptak et al. 2006; Gris e et al. 2008), thus reinforcing the link with a young, high-mass stellar population. However, some ULX counterparts that were initially identified as massive, early-type stars on the basis of their blue colors (*e.g.* Kuntz et al. 2005) are now thought to be low-mass stellar donors and the blue colors due to optical emission from the accretion disk and/or reprocessed radiation from the X-ray source (*e.g.* Copperwheat et al. 2007). Indeed, Tao et al. (2011) have argued that the optical emission from the majority of ULX counterparts is dominated by X-ray reprocessing. However, there have been no unequivocal identifications of low-mass donors in such systems, because we have never had a chance to observe them in quiescence.

In this paper we report the discovery of a ULX that recently erupted in the nearby ( $d = 4.6 \pm 0.2$  Mpc, Saha et al. 2006) grand-design spiral galaxy M83 (NGC 5236), and that we can confirm to be powered by a low-mass companion. The first exposures of a large *Chandra* project to study M83, taken on 23 and 25 December 2010, revealed an unexpected gift: a ULX—a non-nuclear source with a flux comparable to the total circumnuclear flux—that had not appeared in previous *Chandra* images from 2000–01, nor in any other prior X-ray image of M83. The new source appeared  $\sim 1'$  east of the nucleus, well away from the spiral arms and from the many regions with active star formation. Since its discovery, we have monitored the source for a year with *Swift*, and with *Chandra* in our ongoing program observations. We have also obtained optical images of the field containing the ULX from the Gemini South telescope and from the *Hubble Space Telescope* (*HST*), and we find that a new unresolved source, not seen in previous *HST* observations of the same field, has appeared coincident with the ULX.

The remainder of this paper is organized as follows: In §2 we present the new *Chandra* and *Swift* data, along with a brief survey of archival X-ray data where the ULX was absent, and in §3 we give the results of spectroscopic and timing analyses. In §4 we describe the

optical observations and results. In §5 we argue that the M83 ULX is powered by accretion from a low-mass companion that has recently expanded to overflow its Roche lobe, and that the present bright optical emission results from the reprocessing of X-rays in the accretion disk. We go on to discuss the probable geometry and black hole mass in some detail, and close in §6 with a brief summary.

## 2. X-ray Observations

The object was discovered using *Chandra*, whose spectacular angular resolution allowed the quick and definitive determination that no such source appeared in previous X-ray images. The source was discovered when its  $L_{0.3-10} \sim 4 \times 10^{39} \text{ ergs s}^{-1}$ , a ULX by most definitions of that class. The *Chandra* spectrum is unequivocally that of a power-law-like source, but there are many classes of sources with similar spectra, so the nature of the source was not immediately clear. We turned to *Swift* to follow the short-term evolution of the source, and to archival data from other missions to determine what might have been there in the past.

### 2.1. *Chandra* Discovery

The recent *Chandra* data were obtained as part of a detailed study of M83 (Program 12620596; Long P.I.). The data, totalling 729 ks, were obtained in ten observations, each longer than 50 ks. The observations are clustered in December 2010, March 2011, and August 2011, with a final observation in December 2011 (See Table 1.) We used the back-illuminated S3 chip for maximum soft response, since most of the M83 disk fits within its  $8' \times 8'$  field. We carried out the observations in the “very faint” mode for optimum background subtraction. We filtered and analysed the data with standard imaging and spectroscopic tools, such as *dmcopy*, *dmextract* and *speextract*, in the CIAO Version 4.3 (Fruscione et al. 2006) data analysis system.

As shown in the upper right panel of Figure 1, the ULX appears  $\sim 1'$  east of the nucleus of M83. A count-weighted mean of the centroid positions over the first nine observations gives a position

$$\text{R.A. (2000)} = 13^{\text{h}}37^{\text{m}}05^{\text{s}}.135 \pm 0^{\text{s}}.014, \quad \text{Dec. (2000)} = -29^{\circ}52'07''.2 \pm 0''.3$$

(90% confidence level). The root-mean-square scatter of the source positions derived from each *Chandra* observation is  $\sigma \approx 0''.25$ . We also determined a source position using only the five observations during March and April 2011, in which the aimpoint was closest ( $\approx 76''$ )

to the ULX, when the point spread function (PSF) would be most narrow and symmetric, with a 90% encircled energy radius  $\approx 0''.9$ ; we obtained the same result as from the total average, with a root-mean-square scatter  $\sigma \approx 0''.15$ . We confirmed the accuracy of the *Chandra* position further by using two sources in the S3 chip with both X-ray and radio detections: SN1957D (located  $\approx 2'.3$  north-east of the nucleus) and a background radio galaxy ( $\approx 1'$  north-west of the nucleus). The mean X-ray positions of those two sources are within  $\approx 0''.2$  of the radio positions, measured from our Australia Telescope Compact Array observations at 5 GHz; the radio positions have themselves an uncertainty of  $\approx 0''.2$ . We conclude that the mean *Chandra* coordinates can be offset by no more than  $\approx 0''.3$  from the true position.

The two earlier observations of M83, taken with the *Chandra* ACIS-S in 2000 and 2001, do not show the presence of the ULX (see the upper left panel of Figure 1). Applying the Bayesian method of Kraft et al. (1991) to the number of detected counts in the source and background regions, we estimate the net count rate in 2000–2001 to be  $< 1.0 \times 10^{-4}$  ct s $^{-1}$  at the 90% confidence level. This corresponds to an emitted luminosity  $\lesssim 1 \times 10^{36}$  erg s $^{-1}$  for any of the spectral parameter values found in the 2010–2011 series of observations. The newly erupted source had brightened by at least a factor of 3000.

## 2.2. *Swift* Monitoring

After the discovery of the ULX in the *Chandra* data, we monitored it with several series of short ( $\approx 3$  ks) observations with the *Swift* X-ray Telescope (XRT), to follow its short-term evolution.

The ULX is somewhat over  $0'.5$  outside the extended emission from the M83 bulge, in a region free of bright, strongly structured diffuse emission, but in a region where the diffuse emission is still significant, as can be seen in the lower right panel of Figure 1. Thus, we had to choose the background region for photometry from the *Swift* XRT, which has a pixel size of  $2''.4$ , carefully. We set the source region to have a radius of  $18''$ , which contains 70% of the encircled energy at 1 keV, and the background region to be an annulus stretching from  $18''$  to  $35''$ , avoiding several nearby regions of enhanced diffuse emission. The background region contains the extended wings of the ULX, comprising some 14% of the total source flux<sup>2</sup>. Examination of the *Chandra* image for the source and background regions show that both contain several faint point sources; none of these is readily detectable in the *Swift* image,

---

<sup>2</sup> The XRT instrument handbook provides formulae for calculating the encircled energy at 0.5 keV and 4.0 keV. We used these formula to calculate the encircled energy fractions for 0.3–2.0 keV (using the values for 0.5 keV) and for 2.0–10.0 keV (using the values for 4.0 keV).

suggesting that the error produced by not excluding them is on the order of the Poisson statistics of the background. We extracted counts from the source and background regions, solving the simultaneous equations to get the total source counts and the background counts per pixel. Since the exposures were relatively short, the background rate was somewhat uncertain, particularly in bands narrower than the full 0.3–10.0 keV range of the detector. In order to reduce this uncertainty, we determined the mean background rate over all the observations and recalculated the source rates. The difference among individual background rates was small, and the signal-to-noise of the source counts was improved by using the time-averaged background. The resultant light-curve is shown in Fig. 2; the count rate varies from  $\approx 0.03$  to  $\approx 0.07$  count  $s^{-1}$ .

The (2.0–10.0 keV)/(0.3–2.0 keV) hardness ratios, shown in Figure 3, vary significantly among the observations, making the use of a single energy-conversion factor inappropriate. Instead, we calculated the fluxes and hardness ratios expected as a function of power-law index, assuming an absorbed power law with  $N_H = 1.2 \times 10^{21}$   $\text{cm}^{-2}$ , determined from the best-fitting parameters for the December and March *Chandra* data. Then, we used the measured count rates and hardness ratios to produce a flux for each *Swift* observation. The *Swift* light curve in flux units is shown in the right-hand panel of Fig. 2. Even with 3 ks exposures, the total number of counts is insufficient for spectral fitting, and the variation in the hardness ratio argues against summing different observations. We obtained three *Swift* exposures that were nearly simultaneous with *Chandra* exposures. The fluxes calculated from the *Swift* count rates and hardness ratios are roughly consistent with those derived by fitting the *Chandra* spectra, after the latter were corrected for pile-up.

The only earlier *Swift* XRT observation useful for this work was made in 2005. It provides an upper limit of  $F_X(0.3-10 \text{ keV}) < 1.7 \times 10^{-14}$   $\text{ergs cm}^{-2} \text{ s}^{-1}$  ( $L_X(0.3-10 \text{ keV}) < 4.5 \times 10^{37}$   $\text{ergs s}^{-1}$ ), assuming an absorbed power law with  $N_H = 1.2 \times 10^{21}$   $\text{cm}^{-2}$  and  $\Gamma = 2.0$ .

### 2.3. Previous X-ray Observations from Other Missions

M83 has been a popular target in surveys of normal galaxies. As a result there are sufficient data to determine whether the ULX in M83 has been bright in the past.

*XMM-Newton*: Three observations of M83 are available in the public archive. The galaxy is well centered in the field of view of the first of these, from 2003, while in the following two, from 2008, the galaxy falls on a peripheral chip, so the ULX is not covered by all of the instruments in the last two observations. We measured upper limits to the EPIC count rates

using a source region with  $r < 18''$  and a background region with  $18'' < r < 35''$ ; we converted count rates to fluxes assuming an absorbed power law with  $N_H = 1.2 \times 10^{21} \text{ cm}^{-2}$  and  $\Gamma = 2.0$ . If we assume that the source was constant over all the *XMM-Newton* observations, the upper limit becomes  $F_X(0.3\text{--}10.0 \text{ keV}) < 3.9 \times 10^{-15} \text{ ergs cm}^{-2} \text{ s}^{-1}$  ( $L_X(0.3\text{--}10.0 \text{ keV}) < 1.0 \times 10^{37} \text{ ergs s}^{-1}$ ), while the best individual instrument/exposure result is for the PN in 2003 of  $F_X(0.3\text{--}10.0 \text{ keV}) < 7.3 \times 10^{-15} \text{ ergs cm}^{-2} \text{ s}^{-1}$  ( $L_X(0.3\text{--}10.0 \text{ keV}) < 1.8 \times 10^{37} \text{ ergs s}^{-1}$ ).

*ROSAT*: There is one PSPC observation from 1993 and two HRI observations from 1993 and 1994 in the archive, each with exposure time  $\approx 24 \text{ ks}$  (Immler et al. 1999). There is no obvious source at the location of the ULX in the HRI exposures; the detection limit for the combined HRI exposures is  $F_X(0.1\text{--}2.4 \text{ keV}) \approx 10^{-14} \text{ ergs cm}^{-2} \text{ s}^{-1}$  ( $L_X(0.1\text{--}2.4 \text{ keV}) \approx 2.5 \times 10^{37} \text{ ergs s}^{-1}$ ). The nucleus and the ULX are not resolved in the PSPC image. However, since in its ultraluminous state it is comparable to the nucleus in brightness, had the source been ultraluminous during the PSPC observation, one would expect the central source to have had an east-west elongation, which was not observed. Thus we may be reasonably confident that the source was not ultraluminous during the PSPC observation. The same argument can be applied to the *ASCA* observation in February 1994, and the *Einstein* IPC observation in July 1979.

*Einstein*: Besides the IPC observation from 1979, with an exposure time of 6 ks, there are two HRI observations from 1980 and 1981 with exposures of 25 and 20 ks, respectively (Trinchieri et al. 1985). Taking the dimmest detected source in the co-added HRI images from Trinchieri et al. (1985) as an extreme upper limit, we find that the flux is  $F_X < 1.3 \times 10^{-13} \text{ ergs cm}^{-2} \text{ s}^{-1}$  ( $L_X < 3.3 \times 10^{38} \text{ ergs s}^{-1}$ ).

*Summary*: M83 was observed to a depth that would have revealed a ULX, or even a moderately bright ( $L_X > 10^{37} \text{ erg s}^{-1}$ ) X-ray binary in 1979, 1980, 1981, 1993, 1994, 2000, 2001, 2003, 2005, and 2008. The continuously high emission for at least 12 months, from late December 2010 through late December 2011, suggests that if the source has repeated outbursts, they are relatively long. Thus the non-detections over the last three decades suggest that this source is either new or has a long period between ultraluminous episodes.

### 3. X-ray Results

The *Chandra* data are magnificent, providing spectra with  $> 10^4$  counts, but have sparse temporal coverage. The *Swift*/XRT data provide a more complete light-curve, but can provide no more than a hardness ratio. The analysis of each informs and is informed by the other.

### 3.1. Temporal Variation

The *Swift* count rate light-curve in Figure 2 shows that the count rate varied within a range of roughly a factor of two. The data hint at a flux decline since March 2011, which is in agreement with the *Chandra* flux trend. However, given that the source showed flux variations of comparable amplitude during January and February, it may be too early to conclude that the outburst is near its end. The spectral shape, as tracked by the 2.0–10.0 keV/0.3–2.0 keV hardness ratio, is also strongly variable. The count rate versus hardness ratio plot in Figure 3 suggests two different regimes of behavior. In epochs 2 to 5, as defined in Table 1, the hardness ratio varied strongly while the count rate did not, staying within  $\approx 0.03$  to  $0.045$  count s<sup>-1</sup>. In epochs 6 to 13 the hardness ratio did not vary significantly, while the count rate did. After epoch 13 the source returned to the mode seen in the earlier epochs. The broad-band count rate and the hardness ratio are not well-correlated, and do not follow a characteristic track in the hardness-intensity diagram.

The broad-band flux light-curve derived from a combination of *Swift* and *Chandra* observations also fluctuates within a range of roughly a factor of two, between 1 and  $2 \times 10^{-12}$  ergs cm<sup>-2</sup> s<sup>-1</sup>. We determined the *Chandra* fluxes from multicomponent spectral fits. We derived the *Swift* fluxes by assuming a power-law spectrum absorbed by a column of  $1.2 \times 10^{21}$  cm<sup>-2</sup>, constraining the photon index from the hardness ratio, and normalizing the flux to obtain the measured 0.3–10.0 keV band count rate. The full range of flux was spanned by observations in epochs 2 and 3 (a day apart) and by epochs 1 and 2 (9 days apart) and 6 and 7 (11 days apart). There is a hint of greater variability in the observations before mid-February (epoch 8) than after; the clump of observations in March (epochs 9–11) shows little variation in count rate or flux. Unlike the count rate *versus* hardness ratio plot, the flux *versus* hardness ratio plot shows little structure, and the conversion from *Swift* count rates to fluxes adds scatter to the data.

Overall, the source variability during our first 12 months of observations is more similar to the variability seen in ULXs such as Holmberg II X-1 (Grisé et al. 2008) and Holmberg IX X-1 (Kaaret & Feng 2009), than to canonical state transitions, routinely seen in Galactic black hole binaries (Fender et al. 2004; McClintock & Remillard 2006).

We also investigated the intra-observational variability for each *Chandra* epoch. We extracted background-subtracted lightcurves with the CIAO task *dmextract*, and analysed them using the *lcstats*, *efsearch* and *powspec* tasks in FTOOLS (Blackburn 1995). We computed the power spectrum from the shortest period not biased by the Chandra readout rate ( $\sim 10$  s) to the length of the shortest observation ( $\sim 50$  ks). We do not find significant features in the power spectral density over this 0.1 to ( $2 \times 10^{-5}$ ) Hz band for any observation, nor do we see any dips, eclipses or flares. The  $\chi^2$  probability of a constant light-curve is  $\approx 1$  for each

epoch; the Kolmogorov-Smirnoff probability (Kolmogorov 1941) that the flux is constant is  $\gtrsim 7\%$  for all observations except for that of September 2011 (when it is  $\approx 4 \times 10^{-3}$ ). We can only place a  $3\sigma$  upper limit of  $\approx 45\%$  ( $\approx 16\%$ ) to the RMS fractional variation for 10 s (100s) bins at any epoch. Overall, the short-term variability is unremarkable. Heil et al. (2009) has demonstrated that ULXs show a wide variety of short-term variability, including many that show no signs of variability.

### 3.2. X-ray Spectroscopy

For each *Chandra* observation, we extracted source spectra from a circular region with a  $4''$  radius, and background spectra from an annular region between radii of  $6''$  and  $12''$ ; we verified that the background region contains no other point sources and only a negligible amount of diffuse emission. We used the *specextract* script in CIAO Version 4.3 (Fruscione et al. 2006) to build response and area-corrected ancillary response files, and we fitted the spectra in XSPEC Version 12 (Arnaud 1996). Two fully representative examples of the *Chandra* spectra and the fits we carried out are shown in Figure 4.

We fitted the 0.3–10 keV spectrum from each of the *Chandra* observations with two XSPEC models commonly applied to the study of black-hole X-ray binaries: an absorbed disk blackbody (*diskbb*) plus power-law model, and an absorbed thermal Comptonization (*comptt*) model (Titarchuk 1994). The *diskbb* plus *power-law* model in ULXs is typically a good but purely phenomenological test for the presence of a soft excess below 1 keV. Under certain assumptions, the soft excess emission may be attributed to the accretion disk and may be used to constrain the inner disk size. The *comptt* model is a suitable test for mild spectral curvature, in particular at the high energy end of the ACIS bandpass; a characteristic class of ULX spectra with a downturn around 5 keV is formally well fitted with Comptonization models at low plasma temperatures,  $kT_e \approx 1.5$  to 2 keV (Stobbart et al. 2006; Roberts 2007; Gladstone et al. 2009).

The Galactic absorbing foreground column is  $4 \times 10^{20} \text{ cm}^{-2}$  (Kalberla et al. 2005) while the column density due to M83 in this direction is  $1.5 \times 10^{20} \text{ cm}^{-2}$  (using the naturally weighted map from Walter et al. 2008). Thus, other than any internal absorption, the emission should be only lightly absorbed by intervening components. As a result of these considerations, we assumed a fixed Galactic foreground absorption with a column density of  $4 \times 10^{20} \text{ cm}^{-2}$ , and a variable absorption from within M83 and the system itself. These column densities are roughly comparable to the optical extinction (see Section 4.2).

At the observed ACIS-S count rate  $\approx 0.2 \text{ ct s}^{-1}$  (Tables 2 and 3), the source spectra are

affected by pile-up<sup>3</sup>, meaning that there is a high probability that more than one photon falls in a single pixel (or adjacent pixels) between frame readouts. In general, one can correct for the spectral distortions caused by pile-up either by removing pixels with a high pile-up probability from the spectral extraction regions, or by using convolution models during spectral fitting. We started with the latter technique, and used the *pileup* convolution model of Davis (2001) within XSPEC. This model has two principal parameters which can be allowed to vary: the grade migration parameter,  $\alpha$ , and the fraction of the events in the source extraction region to which the pileup will be applied, *psffrac*. When we allowed both of these parameters to vary, we usually found that there were two separate regions of parameter space that fit the *Chandra* spectra. The two model fits implied very different pile-up corrected count rates and different ranges of the  $\alpha$  and the *psffrac* parameters, but otherwise produced the same spectral shape and goodness of fit, as determined by  $\chi^2$ . To break the degeneracy and select the proper range for  $\alpha$  and *psffrac*, we extracted another set of source spectra from annuli that excluded the piled-up central pixels. We then constrained the  $\alpha$  and *psffrac* parameters so that they would produce a spectral fit to the piled-up data that was consistent with the fits to the spectra extracted from the annuli. That this rather involved process produces the correct flux is supported by the several nearly simultaneous *Swift* observations for which the pile-up corrected *Chandra* fluxes are roughly consistent with their *Swift* counterparts.

We find that a *diskbb* component is significantly detected in five of the observations but not the other five (Table 2). Although a cool disk-blackbody component produces a marginal improvement in the  $\chi^2$  for two of those four observations, the F test shows that it is not statistically significant (F-test probability  $P = 0.654$  for the 23 December 2010 observation,  $P = 0.203$  for 4 September 2011). For the 28 December 2011 observation the disk-blackbody produces a significant improvement in the fit (F-test probability  $P = 0.011$ ) although the disk-blackbody component itself is only marginally detected (see Table 2). We see no evidence for a disk-blackbody component in the remaining two observations. A soft excess is detected significantly in the 3 April 2011 observation (F-test probability  $P = 1.1 \times 10^{-3}$ ), but at very low temperatures ( $kT < 0.16$  keV) in an energy range where the ACIS-S3 sensitivity is low and most of the emitted flux is absorbed. Thus, we can neither determine whether that soft excess is a *diskbb* component, nor reliably constrain its characteristic temperature and emission radius.

The absence of a *diskbb* component in some observations cannot be due simply to shorter exposure times. Had such a component always been as strong as during the March 2011

---

<sup>3</sup> [http://cxc.harvard.edu/ciao/download/doc/pileup\\_abc.pdf](http://cxc.harvard.edu/ciao/download/doc/pileup_abc.pdf)

observations, when it accounted for almost half of the emitted X-ray flux, it would have been easily detected at every other epoch. It is implausible that an accretion disk would form, for example, in the two days between 23 and 25 December 2010, or vanish between 29 March and 3 April 2011. Thus, we suggest that the differing significance of the *diskbb* component in various observations more likely depends on the fraction of the inner-disk photons that are upscattered in a rapidly variable Comptonizing medium; it is this upscattering that is probably responsible for the power-law component.

As the observations from March 2011 are those where the *diskbb* component is most prominent, they give us the best direct view of the inner disk, and allow us to use those observations to constrain the disk parameters. The characteristic peak temperatures at those epochs are  $\approx 0.3$  to  $0.4$  keV corresponding to a characteristic inner radius  $r_{\text{in}}/(\cos \theta)^{1/2} \approx 700$  to  $1000$  km. If  $r_{\text{in}}$  corresponds to the innermost stable circular orbit of a face-on Schwarzschild black hole, this value would suggest a black hole mass  $\approx 80$  to  $100M_{\odot}$ , or higher for a fast-spinning black hole. On the other hand, the classical Eddington-luminosity argument provides a lower limit of  $\approx 40M_{\odot}$  for the black hole mass for the same data,  $L_X(0.3 - 10 \text{ keV}) \sim 5 \times 10^{39}$  ergs  $\text{s}^{-1}$ . These two estimates stand in apparent contrast to one another. However, we have no reason to assume that we are seeing disk emission from near the innermost stable circular orbit. If the inner part of the disk is covered by an optically-thick scattering region, the thermal component should come from a larger radius. This is likely to be the case if the mass accretion rate is super-critical, that is above the threshold at which a radiatively-efficient, geometrically-thin disk cannot survive. At such accretion rates (which may be the defining characteristic of ULXs), the inner region may be shrouded by a mass-loaded, optically-thick outflow, and thus the observed temperature of the soft thermal component would be the temperature at the photosphere of such outflow, while the fitted inner-disk radius would be the radius at which the disk begins to be covered or replaced by the outflow (e.g. King & Pounds 2003; Poutanen et al. 2007; Soria 2007; Gladstone et al. 2009). It has been suggested (Gladstone et al. 2009) that a ULX with a lower *diskbb* temperature ( $kT_{\text{in}} \lesssim 0.2$  keV) and relatively weak soft thermal component compared to the hard power-law component will have a stronger outflow and greater mass loading, and thus a lower electron temperature in the wind-dominated, Comptonizing inner region (“warm corona” at  $kT_e \approx 2$  keV), which results in a spectral break at energies  $\sim 5$  keV.

In our case, the power-law component is dominant or comparable to the *diskbb* emission at all epochs. The strong power-law component suggests that the inner disk may indeed remain partly shrouded even in the March 2011 observations, and hence the characteristic masses and sizes based on  $r_{\text{in}}$  must be taken as upper limits. Fitting the spectra with the *comptt* model helps us investigate this issue. For all observations, the *comptt* model provides statistically equivalent fits to the *diskbb* plus *power-law* model. For all except the

23 December 2010 observation, we can place only a lower limit (typically,  $T_e \gtrsim 2$  keV) to the best-fitting electron temperature in the scattering region; this is another way of saying that the power-law-like portion of the spectrum extends beyond the upper limit of the ACIS energy band, without a sharp downturn at least up to  $\approx 7$  keV. To test for the presence of a high-energy spectral break, we fitted the 2.0–10 keV portion of the spectrum with both power-law and broken power-law models, after fixing the pile-up model parameters. We find (Table 4) that a broken power-law model does not improve the fit in any of the *Chandra* observations. The lack of a break in the power-law suggests either that this ULX was not in a slim-disk/optically-thick warm-corona state (Roberts 2007; Gladstone et al. 2009), or that its characteristic coronal temperature was higher than typically found in that variety of ULXs. We conclude that the accretion rate was only moderately super-critical, perhaps not high enough to launch a massive outflow, and that the spectral appearance of this ULX is closer to the “very high state” of Galactic BH transients than to the most extreme examples of warm-corona/outflow sources described in Gladstone et al. (2009).

With only a few exceptions, both the *powerlaw+diskbb* fits and the *comptt* fits indicate that the source has very little internal absorption. The *diskbb* fits suggest intrinsic absorbing column densities  $\sim$  a few times  $10^{20}$  cm $^{-2}$ , somewhat larger than the local H I column,  $1.5 \times 10^{20}$  cm $^{-2}$ ; the *comptt* fits suggest values consistent with no M83 absorption at all.

Finally, we searched for emission lines, either from the ULX itself (*e.g.*, Fe K lines) or from spatially unresolved, X-ray ionized gas in its surroundings. We combined the spectra and their respective response files from all the 2010–2011 *Chandra* observations to increase the signal-to-noise ratio of any possible features. We do not find any significant lines or edges. A narrow 6.4 keV emission line could be added to the local best-fitting continuum, but can have an equivalent width no greater than  $\sim 12$  eV (90% confidence level). Non-detection of either broad or narrow fluorescent Fe lines is not a surprising feature for a ULX (*e.g.*, Goad et al. 2006), although such lines have been detected in the peculiar case of a ULX in M82 (Strickland & Heckman 2007; Dewangan et al. 2006). In general, Fe lines from stellar-mass black holes are weaker than those from AGN (Ross & Fabian 2007), because iron in the inner region of the accretion disk is more highly ionized, and the blurring of the line profile due to Compton scattering is more severe. This is the case in particular when the power-law-like X-ray emission from a scattering corona is comparable to or stronger than the direct thermal emission from the accretion disk—as is the case for most ULXs above 1 keV. If the inner region of the disk is covered or replaced by an optically thick scattering corona (Roberts 2007), we do not expect to see any reflection features. Caballero-García & Fabian (2010) proposed that ULX spectra with a steepening around  $\approx 5$ –7 keV are dominated by a reflection component with a relativistically broadened Fe line; however, this interpretation remains somewhat controversial as it requires *ad hoc* parameters. In any case, the continuum

spectrum of the ULX in M83 does not have such high-energy steepening, either.

In conclusion, had we not had previous observations of M83, the X-ray properties of this source would look like those of any number of ULXs. Its power-law photon index  $\approx 2$ , and its relatively low disk temperature are consistent with average ULX properties (Feng & Soria 2011; Berghea et al. 2008). Flux variability by a factor of a few on timescales of days (and longer) is typical of ULXs (Grisé et al. 2008; Kaaret & Feng 2009), though statistics on that variability are sketchy, and the most closely monitored sources are brighter than this one. Finally, the lack of a disk-dominated phase of the outburst (known as high/soft state in Galactic black holes) is also a typical ULX property (Soria 2011).

#### 4. Optical Counterpart

Optical counterparts of persistent ULXs are typically faint, usually with a B-type star-like appearance at extragalactic distances. When significantly detected, optical variability is only a fraction of a magnitude (e.g., Zampieri et al. 2011) and its physical interpretation is unclear. But in this case, given the proximity of M83 and the dramatic change in the X-ray flux, we have a unique opportunity to investigate and understand the corresponding changes in the optical and UV fluxes. The change was, as expected, below the detectability of the *Swift* UVOT, but was recorded with high confidence by *HST* and ground-based observatories.

##### 4.1. Ground-Based Observations

As part of a previously planned Gemini program, we were able to image the section of M83 containing the ULX from the 8.2-m Gemini-South telescope on 8 April 2011 (UT) (Program # 2011A-0436, Winkler PI). We used the Gemini Multi-Object Spectrograph (GMOS) in its imaging mode, which has a field  $5'.5$  square and  $0''.0728$  pixels. We binned the image  $2 \times 2$  for an effective pixel size of  $0''.146$ , appropriate for the seeing of  $\approx 0''.7$  at the time of our observations. Four filters were used:  $u'$ ,  $g'$ ,  $r'$ , and  $i'$ , with individual exposures of 600, 100, 150, and 200 s, respectively, and with four dithered exposures through each filter. We processed the image data using standard IRAF<sup>4</sup> and Gemini reduction procedures for overscan and bias subtraction, flat-fielding, aligning, and stacking. Flux calibration was done using observations of the spectrophotometric standard LTT 4316 (see Hamuy et al.

---

<sup>4</sup> IRAF is distributed by the National Optical Astronomy Observatories, which is operated by the AURA, Inc., under cooperative agreement with the National Science Foundation.

1992) taken immediately after the M83 images. All observations were at airmass  $< 1.1$ .

A blue stellar object, faint but clearly visible, is present at the position of the ULX in the stacked images in the  $u'$ ,  $g'$ , and  $r'$  bands, and possibly in  $i'$  as well (Figure 5, central panel). Even though the source is located in an inter-arm region well within the innermost spiral arm of M83, the background from the galaxy is complex enough to make accurate photometry of a faint object difficult.

We had previously taken images of M83 with the IMACS instrument on the 6.5-m Magellan I telescope in April 2009 as part of a program to inventory supernova remnants and other nebulae in M83 (Program # 2009A-0446, Winkler PI). These images were taken through narrow-band filters and so are not directly comparable to the 2011 Gemini images, but they nevertheless show fainter stars than the 2011 images because of long exposures and exceptional seeing,  $\approx 0''.4$ . No object at the ULX position is visible in these 2009 images with an upper limit  $m_{5150} \gtrsim 25$  mag. Although the bands are far from identical, we can use the Magellan images (after PSF matching and scaling) to subtract much of the stellar contribution in the Gemini images near the ULX, to produce a background that is far more uniform and thus more amenable to aperture photometry. Figure 5 shows both a Gemini and a Magellan image of the region, together with a difference image that clearly shows the ULX counterpart. From the  $u'$  and  $g'$  images we subtracted the sum of [O III] plus a 200 Å wide continuum band centered at 5200 Å; from the  $r'$  image we subtracted one in a 150 Å wide continuum band centered at 6800 Å. We used these difference images for conventional aperture photometry of the ULX counterpart to obtain the Gemini AB magnitudes given in Table 5. The uncertainties quoted include any due to possible residuals from imperfectly subtracted stars and diffuse background.

## 4.2. *Hubble* Observations

Images with better angular resolution and higher sensitivity for the M83 field containing the ULX were taken in August 2009 with the newly installed WFC3 instrument on *HST* as part of the Early Release Science program (Dopita et al. 2010). Within the error circle of the ULX position, there are no blue sources; the only objects are a few very faint red stars. Following the discovery of the ULX counterpart in the Gemini images, we requested and were awarded two orbits of Director’s Discretionary *HST* time for a second-epoch WFC3 observation, which was carried out on 27 July 2011 (Program 12683, PI: Winkler). The data were processed with the standard WFC3 pipeline, including drizzling of the three dithered frames taken through each of the four filters. The ULX counterpart is readily apparent in the 2011 WFC3 images through the F336W ( $U$ ), F438W ( $B$ ), and F555W ( $V$ ) filters. Alignment

and subtraction of the 2009 *I* image renders the counterpart easily visible on the 2011 F814W (*I*) image as well. The world coordinate systems associated with the WFC3 images at both epochs have been updated to agree with that which we determined for the Magellan images, which in turn was based on several hundred astrometric stars. The position of the ULX counterpart is

$$\text{R.A. (2000.)} = 13^{\text{h}}37^{\text{m}}05.127^{\text{s}}, \quad \text{Decl. (2000.)} = -29^{\circ}52'06.92'' .$$

We estimate the absolute uncertainty in the coordinates to be, at worst,  $0''.1$ , and the registration of all the images relative to one another is better than 10 mas. The difference between the optical and X-ray coordinates is  $0''.28$ , which is well within the combined uncertainty of the X-ray and optical positions. WFC3 images from both the 2009 and the 2011 epochs are shown for a small region directly around the ULX position in Figure 6.

We have carried out photometry of the ULX counterpart and neighboring stars in the WFC3 images using DAOPHOT, consistently taking an aperture with a radius of 2 pixels ( $0''.08$ ) and using standard encircled-energy corrections to account for the missing flux. In the 2009 images, there are a number of very faint red stars quite near the position of the ULX counterpart, though it is not clear if any of them is actually the donor star in quiescence. After updating the world coordinate systems of both images so they are accurately registered, we carried out photometry of the 2009 images using the identical positions and apertures as in 2011 to obtain the limits given in Table 5. While we used standard procedures for the July 2011 observations, we used “forced photometry” at the position of the ULX for the July 2009 data. We did see an excess at the position of the ULX, and these are the values reported in Table 5. However, since there was no specific counterpart at this position, the values represent upper limits to the flux from the counterpart.

As part of an ongoing analysis of the HST data for M83, Hwihyun Kim (private communication) provided photometry and reddening estimates for stars surrounding the ULX position. She determined a mean total extinction of  $A_V = 0.30 \pm 0.34$ . This value indicates modest but variable extinction, consistent with the appearance of the HST imagery. We adopt this mean value for the ULX in correcting the values in Table 5 to obtain intrinsic fluxes. From the WFC3 data we find that the counterpart’s absolute magnitude is  $M_V = -4.85$ , and a total optical luminosity of  $L(3300 - 9000\text{\AA}) \approx 2 \times 10^{37} \text{ ergs s}^{-1}$  at the time of the July 2011 observation. In quiescence, the counterpart was no brighter than  $M_V \approx -2.1$ , and therefore the optical counterpart has brightened optically by a factor of at least 10.

Comparison between the AB magnitudes obtained on 8 April from Gemini and those obtained on 27 July from *HST* (Table 5) indicates no evidence for optical variability over

this period. Further monitoring of the optical source would be valuable, either in tight coordination with X-ray observations, or especially if the X-ray object starts to fade significantly.

## 5. Discussion

We have discovered a bright new source in the low-extinction inter-arm region of M83. Although it is well within the  $D_{25}$  radius, it is still worth considering whether the source could be a background AGN. Using a standard definition of the X-ray/optical flux ratio

$$\log(f_X/f_R) = \log f_X + 5.5 + m_R/2.5$$

(Hornschemeier et al. 2001) where  $f_X$  is the 0.3–10 keV flux and  $m_R$  is the Cousins magnitude, we find for this source, with  $m_R \approx 24$  and  $\log f_X \approx -12$ ,  $\log(f_X/f_R) \approx 3.5$ . This is typical of stellar-mass systems, while AGN have typical  $-1 \lesssim \log(f_X/f_R) \lesssim 1$  (Bauer et al. 2004; Laird et al. 2009). Furthermore, AGN at this flux level are relatively rare (only  $\approx 0.1$  per square degree: Cappelluti et al. 2009) and nearly always have identified optical counterparts. Finally, we are not aware of any AGN that has been observed to vary in X-rays by the factor of at least 3000, as seen for the X-ray source in M83. Thus, it is highly improbable that the source is a background AGN. There are no known historical supernovae in this region, so it is unlikely that the sudden X-ray/optical increase is due to a previously undetected remnant beginning to interact with the circum-stellar medium.

Our discovery of a transient ULX in an interarm region of M83 suggests that the ULX population is more diverse than often assumed. Most ULXs in nearby galaxies are variable sources but have been persistently active throughout the years since their original discovery (typically, with *ROSAT* in the 1990s). Instead, this source was not detected by *Einstein*, *ROSAT*, *XMM-Newton*, nor in previous *Chandra* observations. A flux increase of  $> 3000$  between the 2000–2001 and the 2010–2011 *Chandra* observations is very unusual for a ULX, but it resembles typical behavior of Galactic black hole transients. Its current bright state has lasted at least twelve months, but likely less than two years (based on the faintness of its optical counterpart in the August 2009 *HST* observations). This is longer than most Galactic black hole transients (typically, a few weeks: McClintock & Remillard 2006), but is not unprecedented. For example, the 1996–1997 outburst of GRO J1655–40 lasted for 15 months (Soria et al. 2000), and GRS 1915+105 has remained bright since 1992 (Castro-Tirado 2011).

The other defining characteristic of this ULX is that it is located far from any star-forming region, and it must have a low-mass, evolved donor star (mass  $< 4M_\odot$ ), since no OB counterparts were detected at the ULX position before the start of the outburst (see

§5.2). Irwin et al. (2003, 2004) argued that ULX candidates in the old stellar populations of elliptical galaxies were mostly due to background AGN contamination. In spiral galaxies with mixed populations, ULXs with low mass counterparts had been identified only in a statistical sense (Swartz et al. 2004; Walton et al. 2011). However, our secure identification of this ULX with its optical counterpart confirms the existence of two different classes of ULXs. More specifically, this source is a ULX powered by accretion from a low-mass donor in an older environment within a galaxy with active star formation. This suggests that a classification of ULXs based on the global properties of their host galaxies is incomplete, as it may miss or underestimate a population of older, transient ULXs with short active phases, particularly at the lower reaches of the “ultra-luminous” luminosity range. The presence of older ULXs in star-forming galaxies has long been proposed by Mushotzky (2006). Further evidence for the existence of ULXs with low-mass donors in old stellar populations comes from two transient sources that are only a factor of two less luminous than the new ULX in M83: one in NGC 5128 (Sivakoff et al. 2008) and one in M31 (Kaur et al. 2011).

### 5.1. The Nature of the Accretor

Beginning with Shakura & Sunyaev (1973), a number of steady-state mechanisms have been proposed to allow large super-Eddington accretion rates that lead to much milder super-Eddington luminosities. Galactic black-hole binaries however, with a few exceptions (Jonker & Nelemans 2004), stubbornly remain below the Eddington limit. While it is accepted that ULXs are powered by accreting black holes, the main unsolved issue is whether they contain a different (more massive) kind of black hole than typical Galactic sources, or are simply in a different accretion state (*e.g.*, at a super-Eddington accretion rate). We found that the 0.3–10 keV spectrum of this source is typical of ULXs: dominated by a power-law with a photon index  $\approx 2$  (intermediate between the soft and hard state of Galactic black holes), with an additional soft thermal component at  $kT \approx 0.3$  keV (cooler than typical accretion disks of Galactic black holes). The characteristic inner-disk radius implied by the thermal component is  $\approx 1000$  km: this corresponds to a Schwarzschild black hole mass  $\approx 100 M_{\odot}$  if we are directly seeing the disk all the way to the innermost stable circular orbit, or  $< 100 M_{\odot}$  if the inner disk is hidden by a Comptonizing region. The latter scenario is more likely, given the dominant power-law component. In fact, in some *Chandra* observations the thermal component disappears altogether, which suggests that a larger fraction of the disk emission is Comptonized at such times.

A strict application of the Eddington limit requires a black hole mass  $\gtrsim 40 M_{\odot}$ ; however, luminosities up to  $\sim 3$  times Eddington (implying correspondingly lower black hole masses)

can be produced in standard accretion scenarios. For example, analytical solutions of standard accretion models show that the true emitted luminosity  $\sim (1 + \log \dot{M})$  for  $\dot{M} > 1$  (Poutanen et al. 2007). Recent radiation-magnetohydrodynamic simulations confirm that the isotropic luminosity can reach  $\sim L_{\text{edd}}$  during super-critical accretion (Ohsuga & Mineshige 2011). In addition, mild geometrical beaming can further increase the apparent luminosity by a factor of two for a standard disk seen face-on and by a factor of 10 for supercritical accretion flows (Ohsuga & Mineshige 2011). Observationally, several neutron star X-ray binaries have reached luminosities of a few times Eddington in their flaring state (Bałucińska-Church et al. 2010; Barnard et al. 2003; Homan et al. 2007). Thus, calculated black hole masses may be overestimated by a factor of  $\lesssim 3$ .

It is still an unsolved theoretical problem whether black holes can form from standard stellar evolution at high metallicity (Belczynski et al. 2010; Heger et al. 2003), as metal lines make mass loss more efficient, decreasing the pre-collapse stellar mass drastically. As pointed out in Heger et al. (2003), there are very large uncertainties on exactly what mass/metallicities can actually produce a black hole. It has been argued (Pakull & Mirioni 2002; Mapelli et al. 2009; Zampieri & Roberts 2009) that ULX formation either requires a low-metallicity environment, or is enhanced by a low-metallicity environment (Prestwich et al. 2011). This source demonstrates that low metallicity need not always be the case, since the environment in the inner disk of M83 where the ULX is located can hardly be characterized as a low-metallicity one. Accurate measurements of abundances in regions with relatively high metallicity are notoriously difficult, but recent estimates based on deep spectra of H II regions within the  $D_{25}$  radius give oxygen abundances for a radius of 1'0 from the nucleus to be  $12+\log(\text{O}/\text{H})=8.73\pm 0.01$  (Bresolin et al. 2009), compared to the solar value of 8.69 (Asplund et al. 2005) and the local ISM value of 8.69 (Snow & Witt 1996). A different method applied to the H II regions of M83 produces for the same radius  $12+\log(\text{O}/\text{H})=8.59\pm 0.01$  (Pilyugin et al. 2006) compared to their local ISM reference value of 8.50. While there is some disagreement about the absolute oxygen abundance, it is clear that the relative oxygen abundance for this region is slightly higher than solar. In such an environment, even an older population is unlikely to have a low metallicity, unless the ULX is from a disrupted dwarf galaxy. This object suggests that black holes with masses  $\gtrsim 40 M_{\odot}$  can be found in environments where the local abundance is solar to somewhat super-solar, whereas models suggest that at these abundances only black holes with  $\lesssim 15 M_{\odot}$  are produced (Belczynski et al. 2010). Reducing abundances to LMC values can produce black holes  $\lesssim 30 M_{\odot}$ , so finding a  $\gtrsim 40 M_{\odot}$  black hole in a region with solar abundances, even accounting for enrichment since its stellar formation, is rather unusual and difficult to understand.

## 5.2. The Nature of the Optical Counterpart

The optical colors of the system in outburst are not consistent with a simple blackbody-like spectrum; the flux density, as shown in Fig. 7, decreases from the near-UV to the visible band, but increases again towards the I band. This behavior suggests the presence of at least two components: one peaking in the UV (implying a characteristic blackbody temperature  $\gtrsim 20,000$  K and a characteristic effective radius  $\lesssim 20R_{\odot}$ ) and one in the IR (implying a characteristic blackbody temperature  $\lesssim 4,000$  K and a characteristic effective radius  $\gtrsim 100R_{\odot}$ ). There are (at least) two ways to interpret this situation. One possibility is that the IR emission is dominated by the large outer disk, and the UV excess is the hot spot or the irradiated surface of the donor star. An alternative is that the UV peak is the Rayleigh-Jeans tail of the emission from an irradiated disk and the I-band excess is the Wien tail of the emission from a cool stellar component. In the latter case the disk must be truncated or at least shaded from irradiation beyond  $R \approx 20R_{\odot}$ . If the disk is shaded, there will be no significant emission from beyond  $R \approx 20R_{\odot}$  as the temperature of a non-irradiated disk would be 2000-3000 K (Shakura & Sunyaev 1973; Frank, King & Raine 2002) and would drop rapidly with distance. At those temperatures, the disk gas is entirely neutral, and opacity drops to a minimum (Ferguson et al. 2005). It is still debated whether the outer disk is optically thin or thick to the continuum in that regime (e.g. Cannizzo & Wheeler 1984; Hynes et al. 2005; Idan et al. 2010); however, in either case, its emission should be negligible compared to that from the irradiated part of the disk and the donor star. The pre-outburst optical spectral energy distribution contains only a red component which we suggest is either the donor star or an unrelated red star along the line of sight. When we add to that an irradiated disk model, with disk parameters constrained by the *Chandra* observations of March 2011, we recover the optical brightnesses of the 2011 *HST* observations. Thus we argue that UV/optical emission is due primarily to the irradiated disk, with some stellar contribution in the near-IR.

We used the XSPEC model *diskir* (Gierliński et al. 2009, 2008) to model the irradiated disk emission for the 23 March 2011 *Chandra* data. This observation was chosen because it was the longest, had the best constrained accretion disk parameters, and was made close to the Gemini observations, which we can then tie to the *HST* observations. We verified that the best-fitting disk and power-law parameters obtained with *diskir* for the X-ray data are consistent with the corresponding parameters obtained with our previous fits. The advantage of the *diskir* model over the simpler, more traditional *diskbb* plus *power-law* model is that it allows a more natural extrapolation into the optical band, as the power-law component does not extend beyond the peak of the disk emission. We found that the UV/optical colors of the 2011 *HST* observations are best-fitted with a disk truncation radius  $r_{\text{out}} \approx 11,200$   $r_{\text{in}} \approx 1.4 \times 10^{12}$  cm  $\approx 20R_{\odot}$ , and a fraction of X-ray photons intercepted and re-radiated by the disk to

be  $\approx 5 \times 10^{-3}$ , a very plausible value for irradiated disks in binary systems. Reprocessing fractions between  $\approx 10^{-3}$  and  $\approx 10^{-2}$  are suggested both by theoretical modelling (e.g., Vrtilik et al. 1990; de Jong et al. 1996; King et al. 1997; Dubus et al. 1999) and by observations of accretion disks in Galactic black holes (e.g., Hynes et al. 2002; Gierliński et al. 2009).

The red excesses in both the pre- and post-outburst spectral energy distributions (SEDs) can be represented as a blackbody with  $T \approx 3500$  K and  $\log L/L_\odot \approx 3.5$ , implying a radius  $\approx 150R_\odot$ . This set of parameters is consistent with an AGB star of initial mass  $\approx 2.5\text{--}4M_\odot$  and an age  $\approx 200\text{--}800$  Myr (Padova stellar tracks: Salasnich et al. 2000; Bertelli et al. 2008, 2009; Marigo et al. 2008; Girardi et al. 2010). We do not have enough evidence to determine whether the faint red component comes from the ULX donor star, or from an unrelated evolved star that is projected in the sky within  $0.1''$  of the X-ray source, or even from a positive fluctuation in the background stellar density. There are several other faint red stars in the field (Figure 6). If some of the red emission seen from the optical counterpart when the ULX is in outburst stems from an unrelated star, then the true donor star of the ULX would be even fainter and less massive than we have calculated, but our interpretation of the system remains valid. Even if the red excess is due to a single stellar companion, the parameters given above are descriptive rather than prescriptive; binary evolution is likely to have produced a companion whose structure is somewhat different than an isolated AGB star.

The upper mass/luminosity limits that we place on the optical counterpart are not inconsistent with population studies of the surrounding region. Hwi Hyun Kim (private communication) provided photometry, reddening, and age estimates for the bright stars in a region around the ULX, based on an analysis of the color-color and color-magnitude diagrams. However, none of those stars is close to the ULX ( $r > 60$  pc); the population surrounding the ULX is dominated by an older and fainter population than is accessible by color-color and color-magnitude diagrams, even with *HST*.

If we had observed the optical counterpart *only* in the X-ray luminous state, we would have classified it as a main-sequence early-type B star or a blue supergiant, in agreement with most other ULXs for which a unique optical counterpart has been proposed (Tao et al. 2011). However, in at least one case (Feng & Kaaret 2008; Roberts et al. 2008), it was already suspected that the optical brightness is strongly affected by X-ray irradiation and reprocessing on the stellar surface and/or the outer accretion disk. Here, for the first time we can prove that this is the case because this source is a transient and we have two sets of observations in which the optical brightness is strongly different. It is plausible that some other ULXs with apparently massive donor stars in fact have a low-mass donor and a bright

accretion disk.

### 5.3. The Geometry of the System

The high mass-accretion rate required by the X-ray luminosity, coupled with the low soft-X-ray absorption observed in the X-ray data, imply mass transfer via Roche lobe overflow (as should be the case for most ULXs), and hence the formation of a large accretion disk around the black hole. We have argued that most of the optical emission in outburst is likely to come from the irradiated disk. The required fraction of intercepted X-ray photons is comparable to the typical values inferred for Galactic LMXBs, for which the emission is thought to be quasi-isotropic. We would not expect the same level of reprocessing if most of the X-ray luminosity was beamed along the axis perpendicular to the disk plane. Thus the presence of strong optical reprocessing is further evidence that a ULX is *not* strongly beamed.

Quantitative estimates of the outer disk size and temperature based on broad-band fits to the X-ray/optical spectral energy distribution are somewhat model-dependent; the disk-blackbody component of the X-ray emission varies from epoch to epoch. However, we can obtain useful order-of-magnitude estimates of the system size by applying the empirical relation between optical brightness of an irradiated disk and binary period found by van Paradijs & McClintock (1994):

$$M_V = 1.57 - 1.51 \log P_h - 1.14 \log(L_X/L_{\text{Edd}}),$$

where  $P_h$  is the binary period in hours. In outburst, the absolute visual brightness of the ULX counterpart in the standard (Vegamag) system is  $M_V \approx -4.9$  mag (Table 5, after correcting for line-of-sight extinction). If the X-ray luminosity  $L_X \approx (1-3) \times L_{\text{Edd}}$ , as most classes of ULX models suggest (e.g. Feng & Soria 2011), this corresponds to an orbital period  $\approx 360$  to 830 days. Since the donor star is filling its Roche lobe,  $P_h \rho^{1/2} \approx 10.5$  for mass ratios  $0.01 \lesssim q \lesssim 1$  (Eggleton 1983), where  $\rho$  is the average stellar density in  $\text{g cm}^{-3}$ . Thus, we obtain  $3 \times 10^{-7} \lesssim (\rho/\text{g cm}^{-3}) \lesssim 1.5 \times 10^{-6}$ . These are typical densities of red giants or AGB stars (Salasnich et al. 2000; Bertelli et al. 2008, 2009), consistent with our interpretation of the system. As a comparison, our independent estimate of a mass  $\approx 3M_\odot$  and radius  $\approx 150R_\odot$  for the red star apparently associated with the ULX implies a mean density  $\rho \approx 10^{-6} \text{ g cm}^{-3}$ , in agreement with the expectations if that is the true donor star.

The size of the accretion disk remains uncertain. Using our lowest estimate for  $M_{BH} \sim 40 M_\odot$  and our upper estimate for the  $M_{star} \sim 4 M_\odot$ , the radius of the primary's Roche lobe is at least a few hundred  $R_\odot$ . The maximum size of an accretion disk is  $\approx 80\%$  of

the size of the primary’s Roche lobe (Paczynski 1977; Whitehurst 1988), which corresponds to a characteristic size  $\approx 10^{13}$  cm for this ULX. On the other hand, we have argued that the optical colors and luminosity in outburst suggest an irradiated disk size  $\approx 10^{12}$  cm. One possibility is that the disk is truncated at that radius, in which case the whole disk would be kept ionized by the X-ray illumination. Alternatively, the outer part of the disk may be shaded from irradiation, and therefore much colder, neutral, and not a significant contributor to the optical/IR emission; the temperature of a non-irradiated standard disk (Shakura & Sunyaev 1973) at  $R \approx 10^{13}$  cm would be only  $\approx 600$  K, for the disk parameters fitted to the X-ray emission. We do not have enough information to choose between the two scenarios. Whether the outer disk is mostly ionized or neutral has implications for the transient behavior.

#### 5.4. Transient Behavior

Most Galactic black holes with a low-mass donor star are transient, while most of those with an OB donor are persistent X-ray emitters (albeit with flux and spectral variability). We suggest that the same may be true for ULXs. A few other examples of ULX transients are two sources in NGC 1365 (Soria et al. 2009), one in M 31 (Kaur et al. 2011) two in M 101 (Kuntz et al. 2005), one in NGC 3628 (Strickland et al. 2001), and one in M 82 (Feng & Kaaret 2007). The transient behavior in accreting stellar-mass black holes has been attributed to thermal/viscous disk instabilities (Mineshige & Wheeler 1989; Osaki 1996; Lasota 2001) and/or to mass transfer instabilities (Hameury et al. 1986, 1987, 1988; Viallet & Hameury 2008).

Mass-transfer instabilities operate when the evolved donor star is nearly but not entirely filling its Roche lobe, providing only a low accretion rate and thus producing a low-luminosity “quiescent” state. The resulting X-ray photons penetrate a few Thompson optical depths below the photosphere of the donor star, causing the convective envelope to expand slowly until the star makes full contact with its Roche lobe. This contact dramatically enhances both the mass transfer rate through the L1 point and the X-ray luminosity of the system, which is generally seen as an “outburst” state. However, as a larger accretion disk is formed, it eventually shades the L1 region from X-ray irradiation, decreasing or stopping mass transfer. The parameter space for the mass transfer instability in ULXs is largely unexplored. A necessary condition is that the irradiating X-ray flux at the surface of the donor star be stronger than its intrinsic flux. This is not the case for ULXs with massive donors, but is true for this source and probably for other ULXs with low-mass donors.

In the disk instability model, the disk follows a limit cycle between a hot (higher viscos-

ity) and a cold (lower viscosity) state. The difference between the two states is due to the sudden jump in opacity when the temperature reaches  $\approx 6,500$  K and hydrogen becomes mostly ionized (Cannizzo et al. 1988). The instability can be suppressed if the whole disk is kept ionized by X-ray irradiation (Burderi et al. 1998; King & Ritter 1998; Janiuk & Czerny 2011). For the observed luminosity of the M83 ULX at the peak of the outburst, the outer disk can be kept ionized by irradiation up to a radius  $R_{\text{irr}} \approx 10^{13}(f_{\text{irr}}/10^{-2})^{1/2}$  cm, where  $f_{\text{irr}}$  is the fraction of X-ray flux reprocessed by the disk. From the inferred size of the binary system, the accretion disk can extend beyond this instability boundary if the outer radius reaches the tidal truncation radius (Paczynski 1977; Whitehurst 1988). On the other hand, the observed optical colors suggest that the outer disk of the ULX has a temperature  $\gtrsim 20,000$  K and hence is truncated well inside the tidal radius. Thus, we cannot tell whether the disk instability operates on the ULX in M83 and will be responsible for ultimately bringing the outburst to a close.

If the outburst does end soon, and the X-ray luminosity declines to below  $10^{39}$  erg s $^{-1}$ , we will have a great opportunity to monitor its spectral behavior in the luminosity range typical of Galactic black holes. Determining whether or not a ULX behaves like an ordinary stellar-mass black hole (e.g., similar state transitions and evolution in the hardness-intensity diagram) when its luminosity drops will tell us whether it is powered by an intrinsically different type of black hole, or by an ordinary stellar-mass black hole at an extremely high accretion rate, not usually reached by Galactic black holes.

## 6. Summary

We have discovered a new ULX in M83 using *Chandra*, and have characterized the X-ray properties of the source in a series of *Chandra* and *Swift* observations extending through December 2011. We have also detected the optical counterpart to the source using the Gemini South Telescope and *HST*. The ULX is located in an inter-arm region and well away from sites of active star formation. Its observed properties and our interpretation of them can be summarized as follows:

1. At its discovery in December 2010, the luminosity was  $L_X(0.3 - 10 \text{ keV}) \approx 4 \times 10^{39}$  ergs s $^{-1}$ . The source has remained bright; its luminosity has varied by a factor of two, and it has only recently dropped to  $\approx 2 \times 10^{39}$  ergs s $^{-1}$ . There is no previous evidence for the existence of this X-ray source in observations extending back to 1979; the X-ray flux has increased by at least a factor of 3000.
2. Although there is significant variation between observations, the X-ray light-curves of

individual observations show no signs of short-term variability, nor are there signs of orbital modulations or eclipses.

3. The X-ray spectra can be well fitted by a disk blackbody plus power-law model, or by an absorbed Comptonized spectrum, typical of most ULXs. The strength of the disk blackbody component varies on timescales of days. We attribute this to the fraction of inner disk photons upscattered in a variable Comptonizing region, rather than to a change in the disk.
4. In those X-ray spectra where a disk is evident, the disk luminosity and temperature suggest an inner accretion disk radius of about 1000 km, corresponding to a Schwarzschild black hole with mass  $M_{BH} \approx 100 M_{\odot}$ . The black hole mass could be less if the inner disk is hidden by a Comptonizing region. In order to strictly obey the Eddington limit, the black hole must have a mass  $M_{BH} \gtrsim 40 M_{\odot}$ . However, if we allow the possibility of accretion luminosities up to three times the Eddington limit at super-critical accretion rates, the X-ray data are still consistent with an ordinary stellar-mass black hole.
5. A blue optical counterpart with  $M_V \approx -4.85$  has appeared since August 2009, presumably at the same time as the ULX. The only stars near this site prior to the appearance of the ULX are faint and red, so must belong to an older population. The donor star is not an OB star, and is likely to be a red giant or AGB star with  $M \lesssim 4 M_{\odot}$  and age  $\gtrsim 500$  Myr. We note, however, that had the system been observed only in its luminous state, the donor could easily have been mistakenly interpreted as an OB star, consistent with most other ULXs with uniquely identified optical counterparts. Some of these other ULXs may well have low-mass donor stars as well.
6. During the X-ray outburst, the spectral energy distribution of the optical counterpart is dominated by a blue component, with  $M_V \approx -4.85$  mag, which we interpret as the Rayleigh-Jeans tail of the emission from the outer disk, heated by the X-ray photons. In addition, there is a faint red component that may arise from the surface of the donor star, although we cannot exclude the possibility that it stems from other unrelated stars in the vicinity.
7. The M83 ULX system provides clear evidence that not all ULXs involve an OB donor and a young stellar population, confirming the suggestion from statistical studies that there are two classes of ULXs.
8. The existence of a ULX in the inner disk of M83 suggests that it is possible to produce black holes also in systems with at least solar metallicity.

The ULX in M83 has provided significant insight into the diversity of the ULX population, and provides us with an unequivocal example of a ULX with a low-mass donor. Continued monitoring of this source will bring greater depth of understanding to this source and this class of sources. Determining the length of the current outburst will constrain the extent to which sources like this contribute to the persistent ULX population, and the length of the decline may constrain the size of the accretion disk. It is still actively debated whether ULXs are a state reached by ordinary stellar-mass black holes at extremely high (super-Eddington) accretion rates, or are powered by a different (more massive) type of accreting black hole. Almost all Galactic black hole transients pass through a high/soft state (dominated by thermal disk emission) after the peak of their outburst and before returning to quiescence; they remain in that state for several weeks. If this ULX does the same, the luminosity at which the state changes will help us understand and quantify the relation between stellar-mass black holes and ULXs. If, instead, this ULX continues to behave like a ULX even when its luminosity goes below  $\approx 10^{39}$  erg s $^{-1}$ , then it is likely that there are intrinsic physical differences between the BHs in ULXs and the ordinary stellar-mass black holes. Clearly, this is an interesting object that will continue to illuminate our ignorance about ULXs.

We would like to thank Neil Gehrels and the *Swift* team for approving and supporting our three series of *Swift* DDT observations, and for their flexibility and cooperation in scheduling observations to coincide with those from *Chandra* and *HST*. We would like to thank Matt Mountain, Director of the Space Telescope Science Institute for granting us Director’s Discretionary time for the second-epoch WFC3 observation. We thank Hwi Hyun Kim (Arizona State University) for providing photometry of the HST data in the field surrounding the ULX position. We would also like to thank the referee for a useful referee’s report.

Support for this work was provided by the National Aeronautics and Space Administration through *Chandra* Grant Number G01-12115, issued by the *Chandra* X-ray Observatory Center, which is operated by the Smithsonian Astrophysical Observatory for and on behalf of NASA under contract NAS8-03060. PFW and WPB are grateful for both observing and travel support for the Gemini observations from the Gemini office at NOAO. PFW also acknowledges financial support from the National Science Foundation through grant AST-0908566, and the hospitality of the Research School of Astronomy and Astrophysics, Australian National University, during a portion of the work presented here.

We acknowledge the use of public data from the Swift data archive. This research has made use of data obtained from the High Energy Astrophysics Science Archive Research Center (HEASARC), provided by NASA’s Goddard Space Flight Center.

The Gemini Observatory is operated by AURA under a cooperative agreement with the NSF on behalf of the Gemini partnership: the National Science Foundation (United States), the Science and Technology Facilities Council (United Kingdom), the National Research Council (Canada), CONICYT (Chile), the Australian Research Council (Australia), Ministerio da Ciencia, Tecnologia e Inovation (Brazil) and Ministerio de Ciencia, Tecnologia e Innovacion Productiva (Argentina).

## REFERENCES

- Arnaud, K. A. 1996, in *Astronomical Society of the Pacific Conference Series*, Vol. 101, *Astronomical Data Analysis Software and Systems V*, ed. G. H. Jacoby & J. Barnes, 17
- Asplund, M., Grevesse, N., & Sauval, A. J. 2005, in *Astronomical Society of the Pacific Conference Series*, Vol. 336, *Cosmic Abundances as Records of Stellar Evolution and Nucleosynthesis*, ed. T. G. Barnes III & F. N. Bash, 25
- Bałucińska-Church, M., Gibiec, A., Jackson, N. K., & Church, M. J. 2010, *A&A*, 512, A9
- Barnard, R., Church, M. J., & Bałucińska-Church, M. 2003, *A&A*, 405, 237
- Bauer, F. E., Alexander, D. M., Brandt, W. N., Schneider, D. P., Treister, E., Hornschemeier, A. E., & Garmire, G. P. 2004, *AJ*, 128, 2048
- Begelman, M. C. 2002, *ApJ*, 568, L97
- Begelman, M. C., King, A. R., & Pringle, J. E. 2006, *MNRAS*, 370, 399
- Belczynski, K., Bulik, T., Fryer, C. L., Ruitter, A., Valsecchi, F., Vink, J. S., & Hurley, J. R. 2010, *ApJ*, 714, 1217
- Berghea, C. T., Weaver, K. A., Colbert, E. J. M., & Roberts, T. P. 2008, *ApJ*, 687, 471
- Bertelli, G., Girardi, L., Marigo, P., & Nasi, E. 2008, *A&A*, 484, 815
- Bertelli, G., Nasi, E., Girardi, L., & Marigo, P. 2009, *A&A*, 508, 355
- Blackburn, J. K. 1995, in *Astronomical Society of the Pacific Conference Series*, Vol. 77, *Astronomical Data Analysis Software and Systems IV*, ed. R. A. Shaw, H. E. Payne, & J. J. E. Hayes, 367
- Bresolin, F., Ryan-Weber, E., Kennicutt, R. C., & Goddard, Q. 2009, *ApJ*, 695, 580

- Burderi, L., King, A. R., & Szuszkiewicz, E. 1998, *ApJ*, 509, 85
- Caballero-García, M. D., & Fabian, A. C. 2010, *MNRAS*, 402, 2559
- Cannizzo, J. K., Shafter, A. W., & Wheeler, J. C. 1988, *ApJ*, 333, 227
- Cannizzo, J. K., & Wheeler, J. C. 1984, *ApJS*, 55, 367
- Cappelluti, N., et al. 2009, *A&A*, 497, 635
- Cardelli, J. A., Clayton, G. C., & Mathis, J. S. 1989, *ApJ*, 345, 245
- Castro-Tirado, A. J. 2011, in *IAU Symposium*, Vol. 275, *IAU Symposium*, ed. G. E. Romero, R. A. Sunyaev, & T. Belloni, 270
- Colbert, E. J. M., Heckman, T. M., Ptak, A. F., Strickland, D. K., & Weaver, K. A. 2004, *ApJ*, 602, 231
- Colbert, E. J. M., & Mushotzky, R. F. 1999, *ApJ*, 519, 89
- Copperwheat, C., Cropper, M., Soria, R., & Wu, K. 2007, *MNRAS*, 376, 1407
- Davis, J. E. 2001, *ApJ*, 562, 575
- de Jong, J. A., van Paradijs, J., & Augusteijn, T. 1996, *A&A*, 314, 484
- Dewangan, G. C., Titarchuk, L., & Griffiths, R. E. 2006, *ApJ*, 637, L21
- Dopita, M. A., et al. 2010, *ApJ*, 710, 964
- Dubus, G., Lasota, J.-P., Hameury, J.-M., & Charles, P. 1999, *MNRAS*, 303, 139
- Eggleton, P. P. 1983, *ApJ*, 268, 368
- Fender, R. P., Belloni, T. M., & Gallo, E. 2004, *MNRAS*, 355, 1105
- Feng, H., & Kaaret, P. 2007, *ApJ*, 668, 941
- Feng, H., & Kaaret, P. 2008, *ApJ*, 675, 1067
- Feng, H., & Soria, R. 2011, *ArXiv e-prints*
- Ferguson, J. W., Alexander, D. R., Allard, F., Barman, T., Bodnarik, J. G., Hauschildt, P. H., Heffner-Wong, A., & Tamanai, A. 2005, *ApJ*, 623, 585
- Frank, J., King, A., & Raine, D. J., ed. 2002, *Accretion Power in Astrophysics: Third Edition*

- Fruscione, A., et al. 2006, in Society of Photo-Optical Instrumentation Engineers (SPIE) Conference Series, Vol. 6270, Society of Photo-Optical Instrumentation Engineers (SPIE) Conference Series
- Gierliński, M., Done, C., & Page, K. 2008, MNRAS, 388, 753
- Gierliński, M., Done, C., & Page, K. 2009, MNRAS, 392, 1106
- Girardi, L., et al. 2010, ApJ, 724, 1030
- Gladstone, J. C., Roberts, T. P., & Done, C. 2009, MNRAS, 397, 1836
- Goad, M. R., Roberts, T. P., Reeves, J. N., & Uttley, P. 2006, MNRAS, 365, 191
- Grisé, F., Pakull, M. W., Soria, R., Motch, C., Smith, I. A., Ryder, S. D., & Böttcher, M. 2008, A&A, 486, 151
- Hameury, J. M., King, A. R., & Lasota, J. P. 1986, A&A, 162, 71
- Hameury, J. M., King, A. R., & Lasota, J. P. 1987, A&A, 171, 140
- Hameury, J. M., King, A. R., & Lasota, J. P. 1988, Advances in Space Research, 8, 489
- Hamuy, M., Walker, A. R., Suntzeff, N. B., Gigoux, P., Heathcote, S. R., & Phillips, M. M. 1992, PASP, 104, 533
- Heger, A., Fryer, C. L., Woosley, S. E., Langer, N., & Hartmann, D. H. 2003, ApJ, 591, 288
- Heil, L. M., Vaughan, S., & Roberts, T. P. 2009, MNRAS, 397, 1061
- Homan, J., et al. 2007, ApJ, 656, 420
- Hornschemeier, A. E., et al. 2001, ApJ, 554, 742
- Hynes, R. I., Haswell, C. A., Chaty, S., Shrader, C. R., & Cui, W. 2002, MNRAS, 331, 169
- Hynes, R. I., Robinson, E. L., & Bitner, M. 2005, ApJ, 630, 405
- Idan, I., Lasota, J.-P., Hameury, J.-M., & Shaviv, G. 2010, A&A, 519, A117
- Immler, S., Vogler, A., Ehle, M., & Pietsch, W. 1999, A&A, 352, 415
- Irwin, J. A., Athey, A. E., & Bregman, J. N. 2003, ApJ, 587, 356
- Irwin, J. A., Bregman, J. N., & Athey, A. E. 2004, ApJ, 601, L143

- Janiuk, A., & Czerny, B. 2011, *MNRAS*, 414, 2186
- Jonker, P. G., & Nelemans, G. 2004, *MNRAS*, 354, 355
- Kaaret, P., & Feng, H. 2009, *ApJ*, 702, 1679
- Kalberla, P. M. W., Burton, W. B., Hartmann, D., Arnal, E. M., Bajaja, E., Morras, R., & Pöppel, W. G. L. 2005, *A&A*, 440, 775
- Kaur, A., et al. 2011, ArXiv e-prints
- King, A. R., Davies, M. B., Ward, M. J., Fabbiano, G., & Elvis, M. 2001, *ApJ*, 552, L109
- King, A. R., Kolb, U., & Szuszkiewicz, E. 1997, *ApJ*, 488, 89
- King, A. R., & Pounds, K. A. 2003, *MNRAS*, 345, 657
- King, A. R., & Ritter, H. 1998, *MNRAS*, 293, L42
- Kolmogorov, A. 1941, *Akademiia Nauk SSSR Doklady*, 30, 301
- Kraft, R. P., Burrows, D. N., & Nousek, J. A. 1991, *ApJ*, 374, 344
- Kuntz, K. D., Gruendl, R. A., Chu, Y.-H., Chen, C.-H. R., Still, M., Mukai, K., & Mushotzky, R. F. 2005, *ApJ*, 620, L31
- Laird, E. S., et al. 2009, *ApJS*, 180, 102
- Lasota, J.-P. 2001, in *Black Holes in Binaries and Galactic Nuclei*, ed. L. Kaper, E. P. J. van den Heuvel, & P. A. Woudt, 149
- Liu, J.-F., Bregman, J. N., & Irwin, J. 2006, *ApJ*, 642, 171
- Mapelli, M., Colpi, M., & Zampieri, L. 2009, *MNRAS*, 395, L71
- Marigo, P., Girardi, L., Bressan, A., Groenewegen, M. A. T., Silva, L., & Granato, G. L. 2008, *A&A*, 482, 883
- McClintock, J. E., & Remillard, R. A. 2006, *Black hole binaries*, ed. Lewin, W. H. G. & van der Klis, M. 157
- Mineshige, S., & Wheeler, J. C. 1989, *ApJ*, 343, 241
- Mushotzky, R. 2006, *Advances in Space Research*, 38, 2793
- Ohsuga, K., & Mineshige, S. 2011, *ApJ*, 736, 2

- Osaki, Y. 1996, *PASP*, 108, 39
- Paczynski, B. 1977, *ApJ*, 216, 822
- Pakull, M. W., & Mirioni, L. 2002, in *New Visions of the X-ray Universe in the XMM-Newton and Chandra Era*, 26-30 November 2001, ESTEC, The Netherlands, astro-ph/0202488
- Pilyugin, L. S., Vílchez, J. M., & Thuan, T. X. 2006, *MNRAS*, 370, 1928
- Poutanen, J., Lipunova, G., Fabrika, S., Butkevich, A. G., & Abolmasov, P. 2007, *MNRAS*, 377, 1187
- Prestwich, A. H., Chandar, R., Kuraszkiewicz, J., Zezas, A., Tsantaki, M., Foltz, R., Kalogera, V., & Linden, T. 2011, in *American Astronomical Society Meeting Abstracts #218*, 209.04
- Ptak, A., Colbert, E., van der Marel, R. P., Roye, E., Heckman, T., & Towne, B. 2006, *ApJS*, 166, 154
- Rappaport, S. A., Podsiadlowski, P., & Pfahl, E. 2005, *MNRAS*, 356, 401
- Roberts, T. P. 2007, *Ap&SS*, 311, 203
- Roberts, T. P., Levan, A. J., & Goad, M. R. 2008, *MNRAS*, 387, 73
- Romaniello, M., Panagia, N., Scuderi, S., & Kirshner, R. P. 2002, *AJ*, 123, 915
- Ross, R. R., & Fabian, A. C. 2007, *MNRAS*, 381, 1697
- Saha, A., Thim, F., Tammann, G. A., Reindl, B., & Sandage, A. 2006, *ApJS*, 165, 108
- Salasnich, B., Girardi, L., Weiss, A., & Chiosi, C. 2000, *A&A*, 361, 1023
- Shakura, N. I., & Sunyaev, R. A. 1973, *A&A*, 24, 337
- Sivakoff, G. R., et al. 2008, *ApJ*, 677, L27
- Snow, T. P., & Witt, A. N. 1996, *ApJ*, 468, L65
- Soria, R. 2007, *Ap&SS*, 311, 213
- Soria, R. 2011, *Astronomische Nachrichten*, 332, 330
- Soria, R., Risaliti, G., Elvis, M., Fabbiano, G., Bianchi, S., & Kuncic, Z. 2009, *ApJ*, 695, 1614

- Soria, R., Wu, K., & Hunstead, R. W. 2000, *ApJ*, 539, 445
- Stobart, A.-M., Roberts, T. P., & Wilms, J. 2006, *MNRAS*, 368, 397
- Strickland, D. K., Colbert, E. J. M., Heckman, T. M., Weaver, K. A., Dahlem, M., & Stevens, I. R. 2001, *ApJ*, 560, 707
- Strickland, D. K., & Heckman, T. M. 2007, *ApJ*, 658, 258
- Swartz, D. A., Ghosh, K. K., Tennant, A. F., & Wu, K. 2004, *ApJS*, 154, 519
- Swartz, D. A., Soria, R., Tennant, A. F., & Yukita, M. 2011, *ApJ*, 741, 49
- Tao, L., Feng, H., Grise, F., & Kaaret, P. 2011, *ArXiv e-prints*
- Titarchuk, L. 1994, *ApJ*, 434, 570
- Trinchieri, G., Fabbiano, G., & Palumbo, G. G. C. 1985, *ApJ*, 290, 96
- van Paradijs, J., & McClintock, J. E. 1994, *A&A*, 290, 133
- Viallet, M., & Hameury, J.-M. 2008, *A&A*, 489, 699
- Vrtilek, S. D., Raymond, J. C., Garcia, M. R., Verbunt, F., Hasinger, G., & Kurster, M. 1990, *A&A*, 235, 162
- Walter, F., Brinks, E., de Blok, W. J. G., Bigiel, F., Kennicutt, R. C., Jr., Thornley, M. D., & Leroy, A. 2008, *AJ*, 136, 2563
- Walton, D. J., Roberts, T. P., Mateos, S., & Heard, V. 2011, *MNRAS*, 1147
- Whitehurst, R. 1988, *MNRAS*, 233, 529
- Winter, L. M., Mushotzky, R. F., & Reynolds, C. S. 2006, *ApJ*, 649, 730
- Zampieri, L., Impiombato, D., Falomo, R., Gris e, F., & Soria, R. 2011, *ArXiv e-prints*
- Zampieri, L., & Roberts, T. P. 2009, *MNRAS*, 400, 677

Table 1. M83 X-ray Observations

Epoch	Obsid	Instrument	Date	Exposure (s)	Flux <sup>a</sup> ( $10^{-14}$ erg cm $^{-2}$ s $^{-1}$ )	$L_X$ ( $10^{37}$ erg s $^{-1}$ )
Swift						
	0005605001	XRT	2005-01-24	8592	<1.75	<4.47
2	0031905002	XRT	2011-01-03	399	$114 \pm 33$	$290 \pm 83$
3	0031905003	XRT	2011-01-04	1620	$96 \pm 15$	$245 \pm 39$
4	0031905004	XRT	2011-01-07	2213	$192 \pm 25$	$489 \pm 64$
5	0031905005	XRT	2011-01-11	2140	$139 \pm 19$	$355 \pm 48$
6	0031905006	XRT	2011-01-23	2896	$183 \pm 17$	$465 \pm 44$
7	0031905007	XRT	2011-02-04	2938	$113 \pm 13$	$287 \pm 35$
8	0031905008	XRT	2011-02-16	2882	$222 \pm 18$	$566 \pm 46$
9	0031905009	XRT	2011-02-28	2863	$163 \pm 15$	$415 \pm 39$
10 <sup>b</sup>	0031905010	XRT	2011-03-15	2285	$187 \pm 19$	$476 \pm 48$
11 <sup>c</sup>	0031905011	XRT	2011-03-24	3258	$201 \pm 16$	$513 \pm 40$
12	0031905012	XRT	2011-06-25	3240	$159 \pm 15$	$404 \pm 39$
13	0031905013	XRT	2011-06-30	3146	$147 \pm 15$	$373 \pm 38$
14 <sup>d</sup>	0031905014	XRT	2011-07-27	3588	$94 \pm 11$	$239 \pm 27$
15	0031905015	XRT	2011-08-24	951	$155 \pm 33$	$395 \pm 84$
16 <sup>e</sup>	0031905016	XRT	2011-08-29	2706	$106 \pm 15$	$269 \pm 39$
17	0031905017	XRT	2001-09-04	4048	$118 \pm 12$	$300 \pm 31$
Chandra						
	793	ACIS-S	2000-04-29	50981	< 0.037	< 0.1
	2064	ACIS-S	2001-09-04	9842	...	...
1A	12995	ACIS-S	2010-12-23	59291	120-110	360-300
1B	13202	ACIS-S	2010-12-25	98780	130-120	440-320
10A <sup>b</sup>	12993	ACIS-S	2011-03-15	49398	150-150	450-530
10B	13241	ACIS-S	2011-03-18	78963	160-150	530-410
11A <sup>c</sup>	12994	ACIS-S	2011-03-23	150058	160-150	510-420
11B	12996	ACIS-S	2011-03-29	53044	150-150	530-410
11C	13248	ACIS-S	2011-04-03	54329	150-150	500-400
16 <sup>e</sup>	14332	ACIS-S	2011-08-29	52381	100-100	290-290
18	12992	ACIS-S	2011-09-05	66286	100-100	320-270
19	14342	ACIS-S	2011-12-28	67103	80-80	230-210
XMM-Newton						
	0110910201	MOS1	2003-01-27	21168 <sup>f</sup>	< 0.895	< 2.28
		MOS2		21670	< 0.879	< 2.23
		PN		9668	< 0.728	< 1.85
	0503230101	MOS1	2008-01-16	15946	not in FOV	
		MOS2		16463	< 1.90	< 4.82
		PN		9490	not in FOV	
	0552080101	MOS1	2008-08-16	25413	< 1.50	< 3.82

Table 1—Continued

Epoch	Obsid	Instrument	Date	Exposure (s)	Flux <sup>a</sup> ( $10^{-14}$ erg cm <sup>-2</sup> s <sup>-1</sup> )	$L_X$ ( $10^{37}$ erg s <sup>-1</sup> )
		MOS2		26619	< 1.65	< 4.19
		PN		15706	< 0.988	< 2.51
ROSAT						
	rh600024a01	HRI	1994-07-30	24156	< 1.0 <sup>g</sup>	< 2.54
	rh600024n00	HRI	1993-01-20	23529	...	...
	rp600188a02	PSPC	1993-01-11	23350	... <sup>h</sup>	...
ASCA						
	61016000	SIS	1994-02-12	40186	... <sup>h</sup>	...
Einstein						
	I1334S29.XIA	IPC	1979-07-31	5708	... <sup>h</sup>	...
	H1334S29.XIA	HRI	1980-01-15	20002	< 13 <sup>i</sup>	< 33
	H1334S29.XIB	HRI	1981-02-13	24574	...	...

<sup>a</sup>In 0.3-10.0 keV.

<sup>b</sup>The *Swift* exposure covered the first part of the *Chandra* exposure; the *Swift* exposure lasted from 12:17:32 to 22:05:56 while the *Chandra* exposure began at 12:21:40.

<sup>c</sup>The *Swift* exposure covered the end of the *Chandra* exposure; the *Swift* exposure lasted from 11:20:06 to 21:05:57 while the *Chandra* exposure ended at 22:18:33.

<sup>d</sup>00:34:45 to 03:54:36 This exposure was coincident with the HST exposures in F336E, F438W, F814W. The HST exposure in F555W occurred shortly after the end of the *Swift* exposure.

<sup>e</sup>The *Swift* and *Chandra* exposures were not quite coincident; the *Swift* exposure lasted from 11:35:00 to 15:13:56 while the *Chandra* exposure began at 18:41:51.

<sup>f</sup>After soft proton flare cleaning.

<sup>g</sup>The limiting flux is taken from the  $3\sigma$  limit given by Immler et al. (1999) who combined the two HRI observations for their analysis. The luminosity has been calculated from their flux using the Saha et al. (2006) distance.

<sup>h</sup>The angular resolution was insufficient to separate the ULX from the nuclear emission. However, it should be noted that while in the ULX state, our source has a flux comparable to that of the nucleus, and thus would produce a roughly east-west elongation of the nuclear source. This elongation is not seen for this observation, suggesting that the source was not in an ultraluminous state.

<sup>i</sup>The limiting flux is taken from the analysis of Trinchieri et al. (1985) who combined the two HRI observations before analysis. We have used the smallest detected flux from a point-like source in that study for our limit. The luminosity has been calculated from their flux using the Saha et al. (2006) distance. Visual inspection of the images reveal no source at the location of the ULX in either image.

Table 2. Best-fit power-law+diskbb Model Parameters<sup>a</sup>

Parameter	Value									
	12995	13202	12993	13241	12994	12996	13248	14332	12992	14342
Date	23 Dec	25 Dec	15 Mar	18 Mar	23 Mar	29 Mar	03 Apr	29 Aug	04 Sep	28 Dec
PSFfrac	0.60 <sup>+0.11</sup> <sub>-0.26</sub>	0.58 <sup>+0.11</sup> <sub>-0.16</sub>	0.85 <sup>+0.02</sup> <sub>-0.02</sub>	0.83 <sup>+0.01</sup> <sub>-0.01</sub>	0.84 <sup>+0.01</sup> <sub>-0.01</sub>	0.79 <sup>+0.02</sup> <sub>-0.03</sub>	0.71 <sup>+0.05</sup> <sub>-0.07</sub>	0.71 <sup>+0.15</sup> <sub>-0.30</sub>	0.44 <sup>+0.26</sup> <sub>-0.44</sub>	0.47 <sup>+0.27</sup> <sub>-0.47</sub>
$N_{\text{H}}(10^{20} \text{ cm}^{-2})$	4.3 <sup>+2.8</sup> <sub>-3.0</sub>	9.2 <sup>+4.0</sup> <sub>-3.4</sub>	1.1 <sup>+4.2</sup> <sub>-0.6</sub>	5.4 <sup>+4.8</sup> <sub>-1.2</sub>	3.4 <sup>+0.5</sup> <sub>-2.7</sub>	6.1 <sup>+5.8</sup> <sub>-3.6</sub>	14.8 <sup>+5.7</sup> <sub>-4.1</sub>	3.4 <sup>+2.5</sup> <sub>-2.5</sub>	5.3 <sup>+4.5</sup> <sub>-2.9</sub>	5.2 <sup>+7.3</sup> <sub>-4.1</sub>
$\Gamma$	1.98 <sup>+0.16</sup> <sub>-0.22</sub>	1.89 <sup>+0.15</sup> <sub>-0.14</sub>	1.84 <sup>+0.39</sup> <sub>-0.36</sub>	2.15 <sup>+0.18</sup> <sub>-0.19</sub>	2.09 <sup>+0.23</sup> <sub>-0.23</sub>	2.18 <sup>+0.29</sup> <sub>-0.24</sub>	2.26 <sup>+0.19</sup> <sub>-0.14</sub>	1.82 <sup>+0.18</sup> <sub>-0.17</sub>	1.76 <sup>+0.21</sup> <sub>-0.16</sub>	1.60 <sup>+0.17</sup> <sub>-0.18</sub>
$N_{\text{pl}}(10^{-4} \text{ phot keV}^{-1} \text{ s}^{-1})^{\text{b}}$	2.5 <sup>+0.6</sup> <sub>-0.4</sub>	2.5 <sup>+0.3</sup> <sub>-0.3</sub>	1.7 <sup>+1.9</sup> <sub>-0.9</sub>	2.7 <sup>+2.3</sup> <sub>-1.4</sub>	1.9 <sup>+1.0</sup> <sub>-1.0</sub>	3.1 <sup>+2.0</sup> <sub>-1.5</sub>	4.3 <sup>+0.8</sup> <sub>-0.5</sub>	1.8 <sup>+0.3</sup> <sub>-0.3</sub>	1.8 <sup>+0.4</sup> <sub>-0.3</sub>	1.1 <sup>+0.2</sup> <sub>-0.3</sub>
$kT_{\text{dbb}}(\text{keV})^{\text{c}}$	0.23 <sup>+0.13</sup> <sub>-0.23</sub>	0.18 <sup>+0.05</sup> <sub>-0.03</sub>	0.38 <sup>+0.03</sup> <sub>-0.06</sub>	0.33 <sup>+0.05</sup> <sub>-0.08</sub>	0.33 <sup>+0.04</sup> <sub>-0.02</sub>	0.32 <sup>+0.06</sup> <sub>-0.13</sub>	...	...	0.25 <sup>+0.10</sup> <sub>-0.08</sub>	0.26 <sup>+0.15</sup> <sub>-0.09</sub>
$K_{\text{dbb}}$	1.1 <sup>+9.1</sup> <sub>-1.1</sub>	23.6 <sup>+65.5</sup> <sub>-18.8</sub>	2.3 <sup>+2.3</sup> <sub>-1.1</sub>	3.9 <sup>+1.7</sup> <sub>-1.7</sub>	5.3 <sup>+0.2</sup> <sub>-1.7</sub>	3.3 <sup>+2.1</sup> <sub>-2.0</sub>	...	...	1.5 <sup>+15.6</sup> <sub>-1.4</sub>	1.2 <sup>+16.8</sup> <sub>-1.1</sub>
$\chi^2/\text{dof}$	1.15	0.99	0.94	1.05	1.02	1.15	1.10	0.92	0.94	0.79
$\chi^2$	250.1	275.3	221.2	296.9	316.4	244.6	232.2	151.2	195.8	148.6
dof	217	278	236	284	310	212	211	164	209	187
$C(10^{-1} \text{ cnt s}^{-1})^{\text{de}}$	1.43 <sup>+0.02</sup> <sub>-0.02</sub>	1.50 <sup>+0.01</sup> <sub>-0.01</sub>	1.93 <sup>+0.02</sup> <sub>-0.02</sub>	2.07 <sup>+0.02</sup> <sub>-0.02</sub>	2.13 <sup>+0.01</sup> <sub>-0.01</sub>	2.01 <sup>+0.01</sup> <sub>-0.01</sub>	1.90 <sup>+0.02</sup> <sub>-0.02</sub>	0.98 <sup>+0.01</sup> <sub>-0.01</sub>	1.11 <sup>+0.01</sup> <sub>-0.01</sub>	0.83 <sup>+0.01</sup> <sub>-0.01</sub>
$f(10^{-12} \text{ erg cm}^{-2} \text{ s}^{-1})^{\text{ef}}$	1.2 <sup>+0.1</sup> <sub>-0.1</sub>	1.3 <sup>+0.1</sup> <sub>-0.1</sub>	1.5 <sup>+0.1</sup> <sub>-0.1</sub>	1.6 <sup>+0.1</sup> <sub>-0.1</sub>	1.6 <sup>+0.1</sup> <sub>-0.1</sub>	1.5 <sup>+0.1</sup> <sub>-0.1</sub>	1.5 <sup>+0.1</sup> <sub>-0.1</sub>	1.0 <sup>+0.1</sup> <sub>-0.1</sub>	1.0 <sup>+0.1</sup> <sub>-0.1</sub>	0.8 <sup>+0.1</sup> <sub>-0.1</sub>
$L(10^{39} \text{ erg s}^{-1})^{\text{ef}}$	3.6 <sup>+0.2</sup> <sub>-0.2</sub>	4.4 <sup>+0.5</sup> <sub>-0.4</sub>	4.5 <sup>+0.7</sup> <sub>-0.3</sub>	5.3 <sup>+1.3</sup> <sub>-0.7</sub>	5.1 <sup>+0.5</sup> <sub>-0.4</sub>	5.3 <sup>+1.1</sup> <sub>-0.6</sub>	$\gtrsim 5.0$	2.9 <sup>+0.4</sup> <sub>-0.4</sub>	3.2 <sup>+0.5</sup> <sub>-0.5</sub>	2.3 <sup>+0.3</sup> <sub>-0.2</sub>
$f_{\text{dbb}}^{\text{g}}$	$\lesssim 3\%$	(17 <sup>+7</sup> <sub>-4</sub> )%	(44 <sup>+6</sup> <sub>-17</sub> )%	(36 <sup>+12</sup> <sub>-21</sub> )%	(51 <sup>+7</sup> <sub>-10</sub> )%	(26 <sup>+13</sup> <sub>-14</sub> )%	...	...	(7 <sup>+2</sup> <sub>-6</sub> )%	(9 <sup>+6</sup> <sub>-4</sub> )%

<sup>a</sup>The complete spectral model fitted was  $\text{pileup} \times \text{tbabs}_{\text{Gal}} \times \text{tbabs}_i \times (\text{power-law} + \text{diskbb})$ . All uncertainties are for the 90% confidence interval.

<sup>b</sup>At 1 keV.

<sup>c</sup> $K_{\text{dbb}} = [r_{\text{in}}(\text{km})/d(10 \text{ kpc})]^2 \times \cos \theta$  where  $r_{\text{in}}$  is the apparent inner-disk radius and  $\theta$  the viewing angle.

<sup>d</sup>Before pile-up correction.

<sup>e</sup>In 0.3-10.0 keV.

<sup>f</sup>After pile-up correction.

<sup>g</sup>Fraction of unabsorbed X-ray luminosity in the diskbb component.

Table 3. Best-fit comptt Model Parameters<sup>a</sup>

Parameter	Value									
	12995	13202	12993	13241	12994	12996	13248	14332	12992	14342
Date	23 Dec	25 Dec	15 Mar	18 Mar	23 Mar	29 Mar	03 Apr	29 Aug	04 Sep	28 Dec
PSFfrac	0.59 <sup>+0.11</sup> <sub>-0.17</sub>	0.64 <sup>+0.07</sup> <sub>-0.09</sub>	0.79 <sup>+0.04</sup> <sub>-0.05</sub>	0.77 <sup>+0.03</sup> <sub>-0.03</sub>	0.79 <sup>+0.02</sup> <sub>-0.02</sub>	0.73 <sup>+0.04</sup> <sub>-0.05</sub>	0.75 <sup>+0.05</sup> <sub>-0.06</sub>	0.68 <sup>+0.15</sup> <sub>-0.31</sub>	0.47 <sup>+0.20</sup> <sub>-0.47</sub>	0.42 <sup>+0.29</sup> <sub>-0.42</sub>
$N_{\text{H}}(10^{20} \text{ cm}^{-2})$	< 1.6	< 1.0	7.2 <sup>+2.5</sup> <sub>-7.2</sub>	< 8.0	< 1.2	< 4.9	4.0 <sup>+3.0</sup> <sub>-3.4</sub>	< 4.5	< 3.5	< 3.5
$kT_0$ (keV) <sup>b</sup>	0.11 <sup>+0.02</sup> <sub>-0.01</sub>	0.12 <sup>+0.01</sup> <sub>-0.01</sub>	< 0.12	0.15 <sup>+0.01</sup> <sub>-0.06</sub>	0.14 <sup>+0.01</sup> <sub>-0.01</sub>	0.14 <sup>+0.01</sup> <sub>-0.04</sub>	0.11 <sup>+0.02</sup> <sub>-0.02</sub>	< 0.14	0.13 <sup>+0.02</sup> <sub>-0.03</sub>	0.13 <sup>+0.02</sup> <sub>-0.04</sub>
$kT_e$ (keV) <sup>c</sup>	1.9 <sup>+1.2</sup> <sub>-0.2</sub>	> 2.0	> 6.5	> 1.8	> 1.9	> 1.9	> 2.6	> 1.8	> 1.8	> 2.2
$\tau^{\text{d}}$	7.4 <sup>+0.9</sup> <sub>-0.3</sub>	< 8.3	1.8 <sup>+5.3</sup> <sub>-0.5</sub>	5.0 <sup>+2.6</sup> <sub>-2.7</sub>	4.9 <sup>+1.4</sup> <sub>-0.7</sub>	5.0 <sup>+2.3</sup> <sub>-1.1</sub>	0.7 <sup>+3.9</sup> <sub>-0.3</sub>	3.2 <sup>+16.4</sup> <sub>-0.6</sub>	7.6 <sup>+0.7</sup> <sub>-1.5</sub>	5.9 <sup>+1.7</sup> <sub>-1.6</sub>
$K_{\text{c}}^{\text{e}}$	4.5 <sup>+1.2</sup> <sub>-1.9</sub>	3.5 <sup>+1.2</sup> <sub>-*</sub>	2.8 <sup>+*</sup> <sub>-*</sub>	5.6 <sup>+6.0</sup> <sub>-*</sub>	6.9 <sup>+0.7</sup> <sub>-*</sub>	4.9 <sup>+4.3</sup> <sub>-*</sub>	0.3 <sup>+1.0</sup> <sub>-*</sub>	0.4 <sup>+*</sup> <sub>-*</sub>	2.7 <sup>+4.2</sup> <sub>-*</sub>	1.0 <sup>+4.2</sup> <sub>-*</sub>
$\chi^2/\text{dof}$	1.10	0.95	0.97	1.04	1.05	1.15	1.10	0.93	0.93	0.81
$\chi^2$	239.2	263.5	229.5	294.5	325.2	242.7	231.3	151.4	194.8	151.1
dof	217	278	236	284	310	212	211	162	209	187
$C$ ( $10^{-1} \text{ cnt s}^{-1}$ ) <sup>gh</sup>	1.43 ± 0.02	1.50 <sup>+0.01</sup> <sub>-0.01</sub>	1.93 <sup>+0.02</sup> <sub>-0.02</sub>	2.07 <sup>+0.02</sup> <sub>-0.02</sub>	2.13 <sup>+0.01</sup> <sub>-0.01</sub>	2.01 <sup>+0.01</sup> <sub>-0.01</sub>	1.90 <sup>+0.02</sup> <sub>-0.02</sub>	0.98 <sup>+0.01</sup> <sub>-0.01</sub>	1.11 <sup>+0.01</sup> <sub>-0.01</sub>	0.83 <sup>+0.01</sup> <sub>-0.01</sub>
$f$ ( $\text{erg cm}^{-2} \text{ s}^{-1}$ ) <sup>hi</sup>	1.1 <sup>+0.1</sup> <sub>-0.1</sub>	1.2 <sup>+0.1</sup> <sub>-0.1</sub>	1.5 <sup>+0.1</sup> <sub>-0.1</sub>	1.0 <sup>+0.1</sup> <sub>-0.1</sub>	1.0 <sup>+0.1</sup> <sub>-0.1</sub>	0.8 <sup>+0.1</sup> <sub>-0.1</sub>				
$L$ ( $10^{39} \text{ erg s}^{-1}$ ) <sup>hj</sup>	3.0 <sup>+0.1</sup> <sub>-0.1</sub>	3.2 <sup>+0.1</sup> <sub>-0.1</sub>	5.3 <sup>+0.5</sup> <sub>-1.2</sub>	4.1 <sup>+1.4</sup> <sub>-0.1</sub>	4.2 <sup>+0.2</sup> <sub>-0.2</sub>	4.1 <sup>+0.6</sup> <sub>-0.2</sub>	4.0 <sup>+0.9</sup> <sub>-0.1</sub>	2.9 <sup>+0.4</sup> <sub>-0.4</sub>	2.7 <sup>+0.2</sup> <sub>-0.2</sub>	2.1 <sup>+0.2</sup> <sub>-0.2</sub>

<sup>a</sup>The complete spectral model fitted was pileup × tbabs<sub>Gal</sub> × tbabs<sub>i</sub> × (comptt). All uncertainties are for the 90% confidence interval.

<sup>b</sup>Seed photon temperature.

<sup>c</sup>Plasma temperature.

<sup>d</sup>Scattering optical depth.

<sup>e</sup>Normalization in  $10^{-4}$  XSPEC units (Titarchuk 1994).

<sup>f</sup>Uncertainty does not converge as the temperature is unconstrained.

<sup>g</sup>Before pile-up correction.

<sup>h</sup>In 0.3-10.0 keV.

<sup>i</sup>After pile-up correction.

<sup>j</sup>Unabsorbed luminosity.

Table 4. Best-fit Power-Law Over the 2–10 keV Band

Parameter	Value									
	12995	13202	12993	13241	12994	12996	13248	14332	12992	14342
$\Gamma$	$2.05^{+0.10}_{-0.13}$	$1.97^{+0.13}_{-0.06}$	$2.50^{+0.10}_{-0.12}$	$2.61^{+0.08}_{-0.09}$	$2.73^{+0.06}_{-0.06}$	$2.45^{+0.14}_{-0.08}$	$2.36^{+0.08}_{-0.13}$	$1.84^{+0.14}_{-0.13}$	$1.85^{+0.16}_{-0.10}$	$1.61^{+0.33}_{-0.13}$
$\chi^2_\nu$	1.06	0.90	0.85	1.12	0.97	1.13	1.05	0.91	0.84	0.81
$\chi^2$	114.58	151.62	108.22	195.85	194.40	117.19	109.25	56.4	86.6	66.1
dof	108	168	128	175	201	104	104	62	103	82
$\Gamma_1$	$1.99^{+0.11}_{-0.17}$	$1.94^{+0.10}_{-0.09}$	NA <sup>a</sup>	NA						
$E_{\text{br}}$ (keV)	$5.3^{+3.2}_{-3.7}$	$6.0^{+0.7}_{-2.0}$	NA							
$\Gamma_2$	$3.14^{+4.48}_{-1.29}$	$4.56^{+*}_{-2.41}$	NA							
$\chi^2_\nu$	1.06	0.88	NA							
$\chi^2$	111.92	146.74	NA							
dof	106	166	NA							
F test	$P = 0.288$	$P = 0.066$	NA							

<sup>a</sup>Broken power-law models with the constraint that  $\Gamma_2 > \Gamma_1$  do not provide any improvement to the  $\chi^2_\nu$  value.

Table 5. Observations of the Optical Counterpart to the M83 ULX

Date	Telescope	Instrument	Exposure (s)	Filter			Magnitude <sup>a</sup>	A( $\lambda$ ) <sup>b</sup> (mag)	Unabsorbed Flux (Jy) <sup>c</sup>
				Band	$\lambda_c$ (Å)	$\Delta\lambda$ (Å)			
2009 Apr 26	Magellan I	IMACS	$7 \times 600$	[O III]	5007	50			
2009 Apr 26	Magellan I	IMACS	$7 \times 200$	Green Cont'm	5316	161	$m_{5150} \gtrsim 25.0$		
2009 Apr 26	Magellan I	IMACS	$7 \times 200$	Red Cont'm	6815	216			
2009 Aug 9	<i>HST</i>	WFC3	$3 \times 630$	<i>U</i> (F336W)	3355	511	$m_{3355} = 28.1 \pm 0.8^c$	0.48	$3.2 \times 10^{-8}$
2009 Aug 9	<i>HST</i>	WFC3	$3 \times 640$	<i>B</i> (F438W)	4326	618	$m_{4326} = 27.5 \pm 0.6^c$	0.40	$5.4 \times 10^{-8}$
2009 Aug 9	<i>HST</i>	WFC3	$3 \times 401$	<i>V</i> (F555W)	5308	1562	$m_{5308} = 26.4 \pm 0.3^c$	0.30	$1.3 \times 10^{-7}$
2009 Aug 9	<i>HST</i>	WFC3	$3 \times 401$	<i>I</i> (F814W)	8030	1536	$m_{8030} = 24.4 \pm 0.3^c$	0.18	$7.7 \times 10^{-7}$
2011 Apr 8	Gemini-S	GMOS	$4 \times 600$	<i>u'</i>	3650	490	$m_{3650} = 23.4 \pm 0.3$	0.47	$2.4 \times 10^{-6}$
2011 Apr 8	Gemini-S	GMOS	$4 \times 100$	<i>g'</i>	4780	1540	$m_{4780} = 23.8 \pm 0.2$	0.35	$1.6 \times 10^{-6}$
2011 Apr 8	Gemini-S	GMOS	$4 \times 150$	<i>r'</i>	6340	1440	$m_{6340} = 23.8 \pm 0.3$	0.25	$1.4 \times 10^{-6}$
2011 July 27	<i>HST</i>	WFC3	$3 \times 608$	<i>U</i> (F336W)	3355	511	$m_{3355} = 23.18 \pm 0.08$	0.48	$2.0 \times 10^{-6}$
2011 July 27	<i>HST</i>	WFC3	$3 \times 330$	<i>B</i> (F438W)	4326	618	$m_{4326} = 23.71 \pm 0.06$	0.40	$1.7 \times 10^{-6}$
2011 July 27	<i>HST</i>	WFC3	$3 \times 245$	<i>V</i> (F555W)	5308	1562	$m_{5308} = 23.73 \pm 0.05$	0.30	$1.6 \times 10^{-6}$
2011 July 27	<i>HST</i>	WFC3	$3 \times 487$	<i>I</i> (F814W)	8030	1536	$m_{8030} = 23.87 \pm 0.06$	0.18	$1.7 \times 10^{-6}$

<sup>a</sup>All magnitudes are observed AB magnitudes at the central wavelength. For WFC3, these use the nominal WFC3 zero points given at [http://www.stsci.edu/hst/wfc3/phot\\_zp\\_lbn](http://www.stsci.edu/hst/wfc3/phot_zp_lbn).

<sup>b</sup>Assuming  $A_V = 0.30$  and using reddening corrections from Romaniello et al. (2002) for the HST filters and from Cardelli et al. (1989) at the central wavelengths for the Gemini filters.

<sup>c</sup>Values obtained from the 2009 *HST* observations correspond to the excess flux at the location of the ULX and are upper limits to the flux of the pre-outburst donor star.

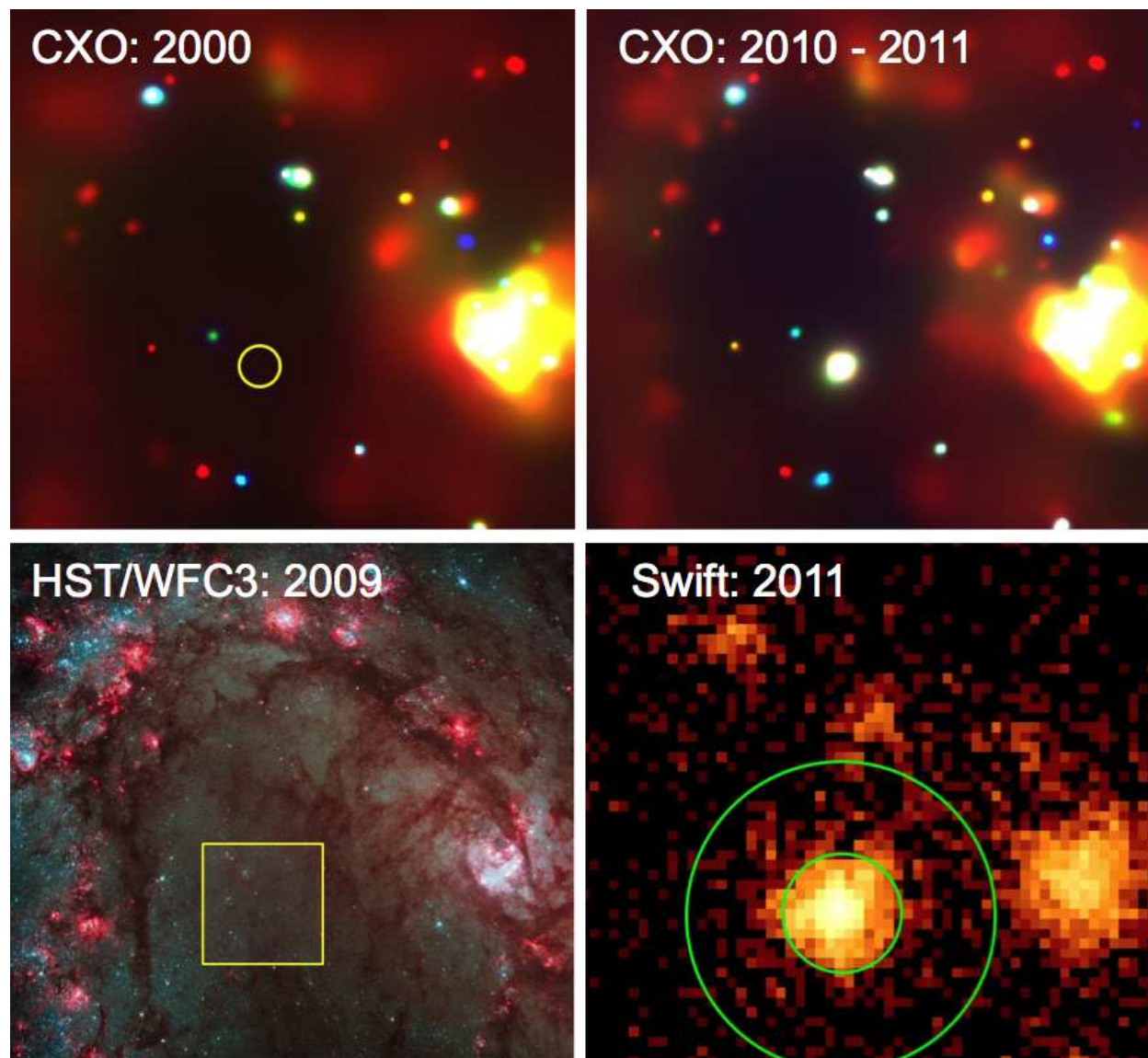


Fig. 1.— **Upper Left:** X-ray image of the inner region of M83, from the *Chandra* observation in 2000. Color coding: red, 0.3–1.0 keV; green, 1.0–2.0 keV; blue, 2.0–7.0 keV. The yellow circle encloses the position of the ULX. **Upper Right:** X-ray image of the same region from our 2010–2011 *Chandra* observations, showing the newly discovered ULX. Color coding is as in the upper left panel. **Lower Left:** Optical color composite image of approximately the same region from the 2009 *HST*/WFC3 Early Release Science data. The diffuse red emission is from  $H\alpha$  and U, V, and I bands are shown as blue, green, and red. The  $30'' \times 30''$  yellow box is shown in greater detail in Figure 5. **Lower Right:** The co-added *Swift* image in the 0.3–10.0 keV band. The source and background regions used for the photometry are shown. Each panel is just over  $2'$  on a side and the physical size of each panel is  $\approx 2.7$  kpc. North is up, East is left.

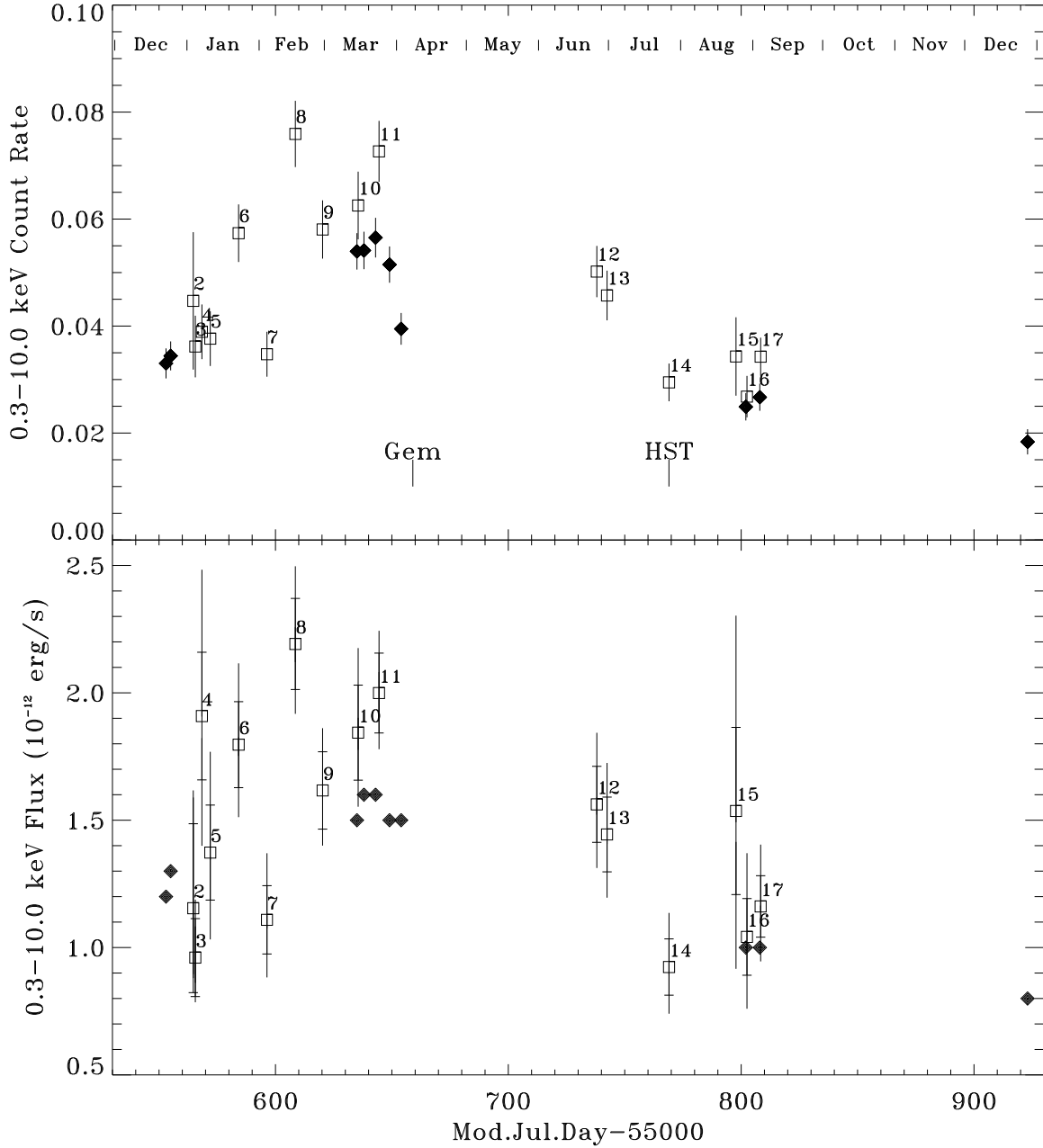


Fig. 2.— **Top:** The *Swift* 0.3–10.0 keV count rate as a function of time. The open boxes are the *Swift* points labeled by their epoch. The filled diamonds are the *Chandra* *powerlaw+diskbb* spectral fits converted to *Swift* count rates. The dates of the Gemini and *HST* observations are also marked. **Bottom:** The flux as a function of time. The open boxes are the *Swift* count rates converted to fluxes as described in the text. The filled diamonds are the *Chandra* fluxes derived from the *powerlaw+diskbb* spectral fits.

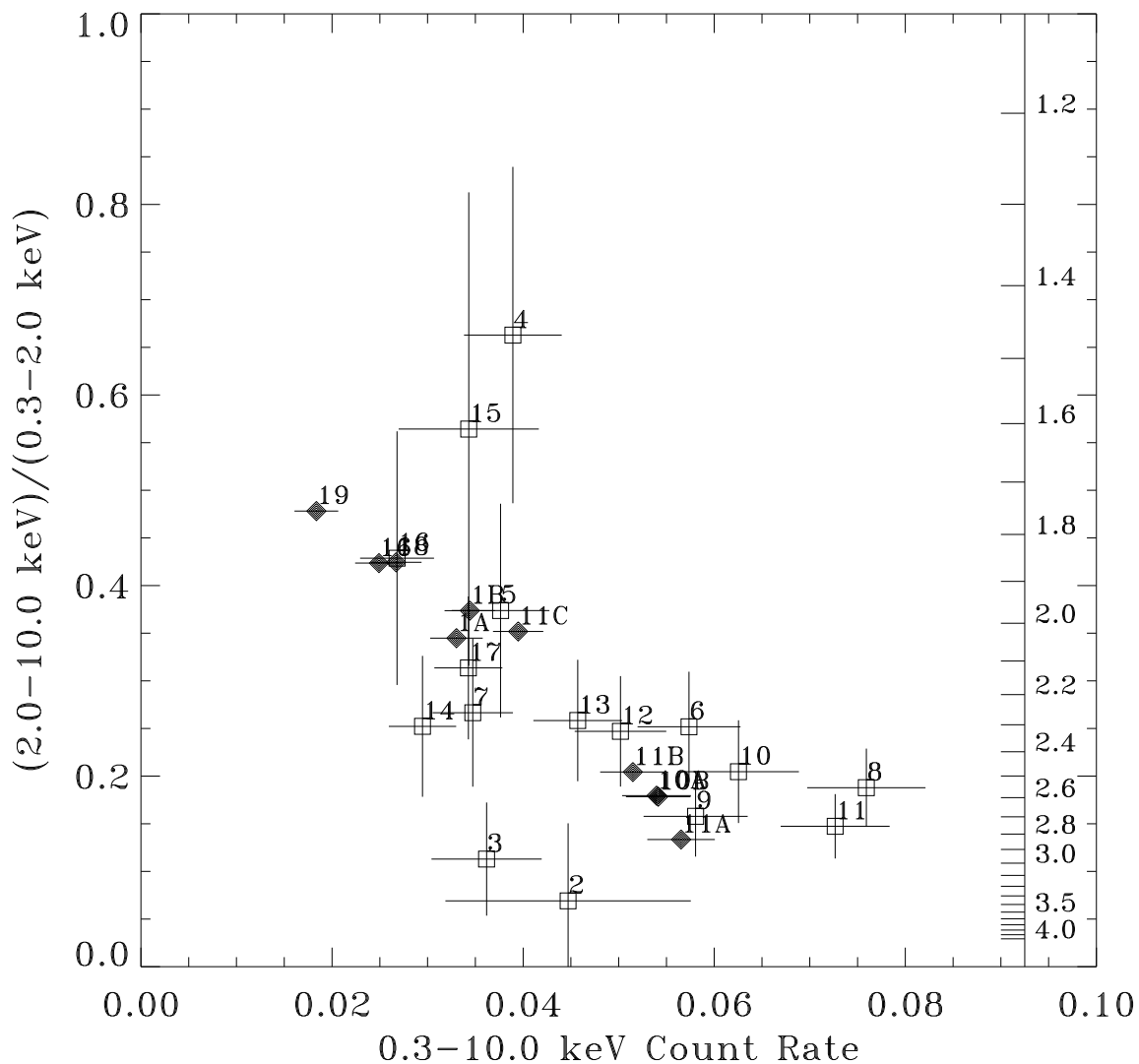


Fig. 3.— The 2.0–10.0 keV/0.3–2.0 keV hardness ratio as a function of the 0.3–10.0 keV band count rate. The scale on the right is the equivalent power law index, assuming a simple absorbed power law with an  $N(\text{H})$  of  $1.2 \times 10^{21} \text{ cm}^{-2}$ . The points are labeled by their epoch. The open boxes are the *Swift* data points labeled by their epoch. The filled diamonds are the *Chandra powerlaw+diskbb* spectral fits converted to the *Swift* count rates and hardness ratios.

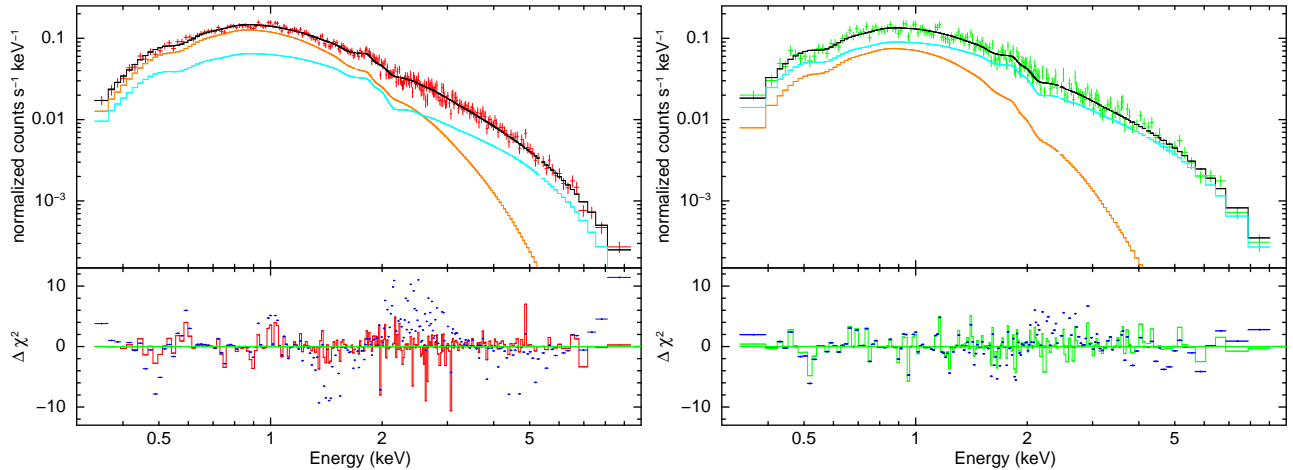


Fig. 4.— **Left:** The 23 March 2011 *Chandra*/ACIS spectrum fitted with an absorbed *diskbb* plus *powerlaw* model, convolved with a *pileup* model. The data points (in red) are binned to a signal-to-noise ratio  $> 7$  for display purposes only. **Top panel:** The separate contributions of the two model components (*diskbb* in orange, *powerlaw* in cyan). **Bottom panel:** The  $\chi^2$  residuals for the best-fitting model with pile-up correction (red stepped line), as well as without pile-up correction (blue data points). See Table 2 for the best-fitting parameters. **Right:** As in the left panel but for the 29 March 2011 spectrum. The data points (in green) are binned to a signal-to-noise ratio  $> 5$  for display purpose only. See Table 2 for the best-fitting parameters. Note the change in relative strength of the fit components.

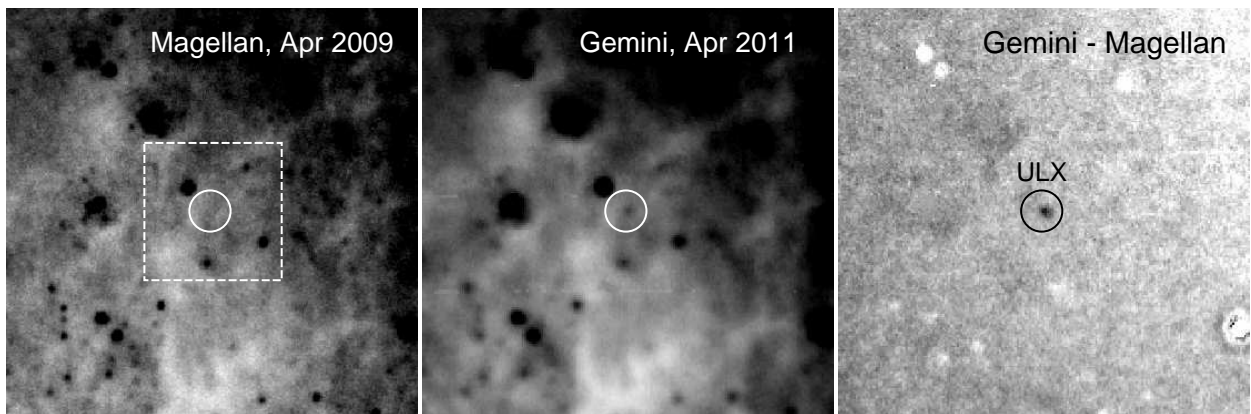


Fig. 5.— Images showing a  $30''$  square region centered on the position of the ULX (the  $3''$  diameter circle) from **Left:** Magellan IMACS, ( $[\text{O III}]$  plus narrow green continuum) from April 2009, **Center:** Gemini-S GMOS, ( $g$ ) from April 2011, and **Right:** the difference image between the Gemini image and the Magellan one after PSF-matching and scaling. North is up and east to the left; the dashed box indicates the  $10''$  field shown in Fig. 6.

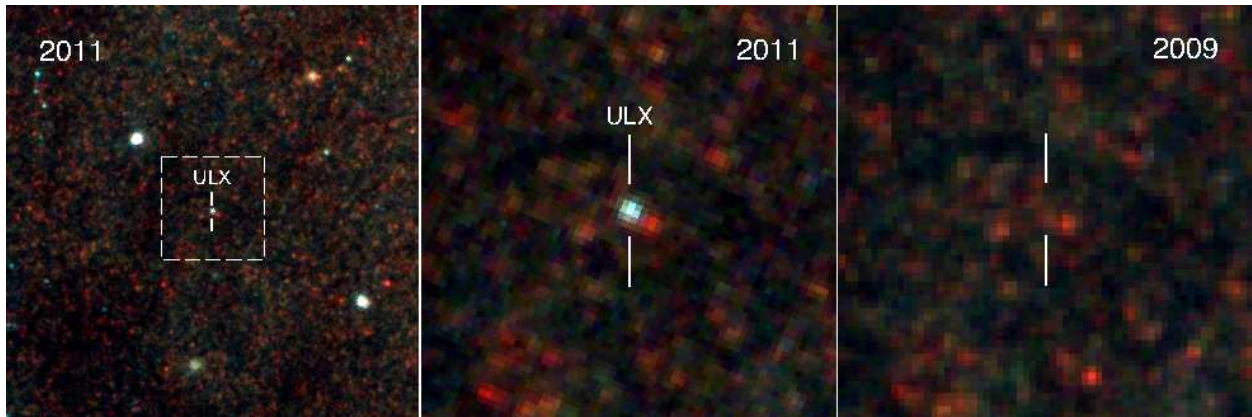


Fig. 6.— *HST* WFC3 true-color images of the region around the ULX. In all panels, the colors are: blue, for the F438W filter; green, for F555W; and red, for F814W. North is up and East to the left. **Left:** Image from July 2011, during the X-ray luminous state; the ULX counterpart appears distinctly blue. The field size is  $10''$  square. This panel can be compared to the ground-based images in the previous figure. The dashed box shows the region covered by the next two panels. **Middle:** A  $2''.5$  by  $2''.5$  detail of the July 2011 image. **Right:** Image from August 2009, at the same scale as the previous panel. The bright blue “star” is not present; there are many faint red stars near the ULX position in the 2009 image, but none is exactly coincident.

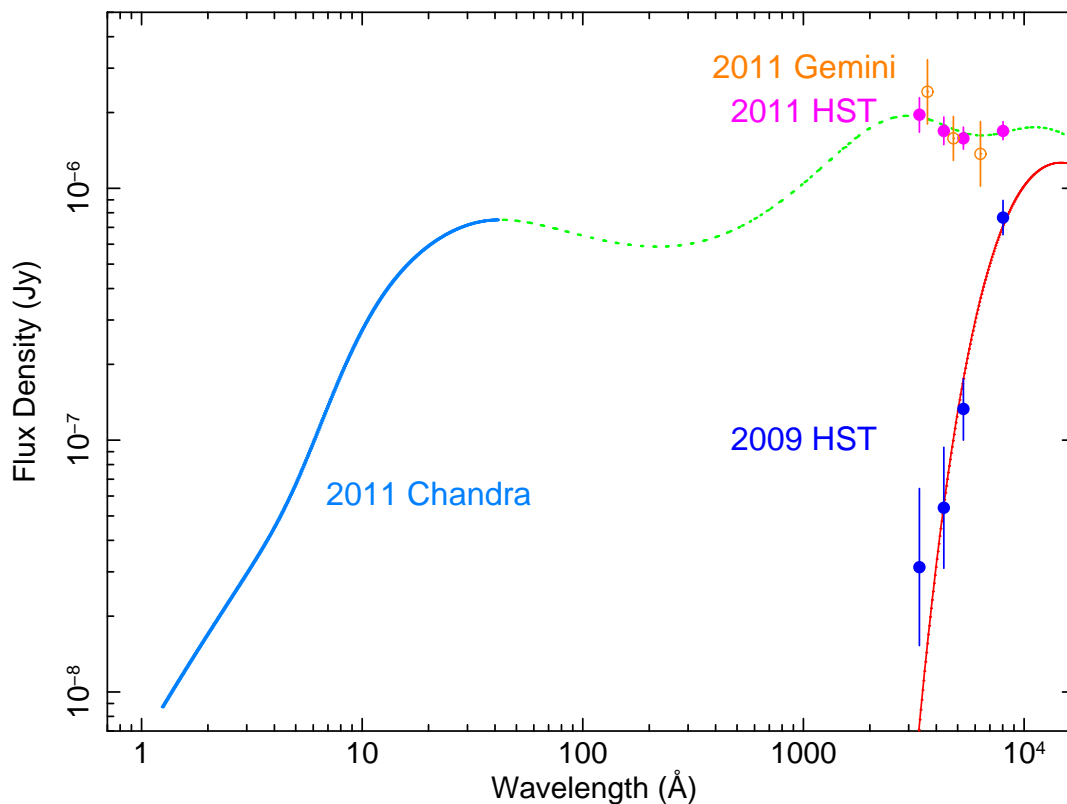


Fig. 7.— Model of the multi-wavelength spectral energy distribution (SED) in outburst and quiescence. The **blue** curve at short wavelengths is the 0.3–10 keV best fit *diskir* model for the 23 March 2011 *Chandra* data, which were chosen for this exercise as they are from the longest observation with the strongest constraints on the accretion disk parameters. The **dark blue** data points are the pre-outburst *HST* measurements from 9 August 2009. These are actually upper limits for the flux from any actual counterpart. The **red** curve is the best fit assuming that the upper limits to the light from the pre-outburst star actually correspond to the light from that star. The **magenta** data points are from the 27 July 2011 *HST* measurements; the **orange** data points are from the 8 April 2011 Gemini measurements; and the **green** dotted line is the modeled emission from an irradiated disk with the addition of the pre-outburst blackbody. All data and models have been corrected for absorption/extinction.